Atlantic Warm Pool Variability in the CMIP5 Simulations

HAILONG LIU

Cooperative Institute for Marine and Atmospheric Studies, University of Miami, and Atlantic Oceanographic and Meteorological Laboratory, NOAA, Miami, Florida

CHUNZAI WANG

Atlantic Oceanographic and Meteorological Laboratory, NOAA, Miami, Florida

SANG-KI LEE AND DAVID ENFIELD

Cooperative Institute for Marine and Atmospheric Studies, University of Miami, and Atlantic Oceanographic and Meteorological Laboratory, NOAA, Miami, Florida

(Manuscript received 31 July 2012, in final form 12 December 2012)

ABSTRACT

This study investigates Atlantic warm pool (AWP) variability in the historical run of 19 coupled general circulation models (CGCMs) submitted to phase 5 of the Coupled Model Intercomparison Project (CMIP5). As with the CGCMs in phase 3 (CMIP3), most models suffer from the cold SST bias in the AWP region and also show very weak AWP variability as represented by the AWP area index. However, for the seasonal cycle the AWP SST bias of model ensemble and model sensitivities are decreased compared with CMIP3, indicating that the CGCMs are improved. The origin of the cold SST bias in the AWP region remains unknown, but among the CGCMs in CMIP5 excess (insufficient) high-level cloud simulation decreases (enhances) the cold SST bias in the AWP region through the warming effect of the high-level cloud radiative forcing. Thus, the AWP SST bias in CMIP5 is more modulated by an erroneous radiation balance due to misrepresentation of high-level clouds rather than low-level clouds as in CMIP3. AWP variability is assessed as in the authors' previous study in the aspects of spectral analysis, interannual variability, multidecadal variability, and comparison of the remote connections with ENSO and the North Atlantic Oscillation (NAO) against observations. In observations the maximum influences of the NAO and ENSO on the AWP take place in boreal spring. For some CGCMs these influences erroneously last to late summer. The effect of this overestimated remote forcing can be seen in the variability statistics as shown in the rotated EOF patterns from the models. It is concluded that the NCAR Community Climate System Model, version 4 (CCSM4), the Goddard Institute for Space Studies (GISS) Model E, version 2, coupled with the Hybrid Coordinate Ocean Model (HYCOM) ocean model (GISS-E2H), and the GISS Model E, version 2, coupled with the Russell ocean model (GISS-E2R) are the best three models of CMIP5 in simulating AWP variability.

1. Introduction

The Atlantic warm pool (AWP), defined as the region with sea surface temperature (SST) above 28.5°C consisting of the Gulf of Mexico, the Caribbean Sea, and the western tropical North Atlantic, undergoes strong variations on seasonal to multidecadal time scales (Wang and Enfield 2001, 2003; Wang et al. 2008a,b; Enfield and Cid-Serrano 2010). The AWP variability has been shown to play a role in the climate system by affecting precipitation patterns and tropical cyclone activity (Wang et al. 2006, 2008a,b, 2011), so it is important to evaluate how well coupled general circulation models (CGCMs) represent this variability. Liu et al. (2012, hereafter LWLE12) have studied the AWP variability against observations in 22 CGCMs from phase 3 of the Coupled Model Intercomparison Project (CMIP3), concluding that most CMIP3 CGCMs suffer from a marked cold SST bias in the AWP region but that there is always one group of CGCMs that is able to represent well each aspect of AWP variability, although each aspect is reproduced by a different set of models. This paper extends the AWP variability study in

Corresponding author address: Hailong Liu, RSMAS/CIMAS, 4600 Rickenbacker Causeway, Miami, FL 33149.
E-mail: hailong.liu@noaa.gov

DOI: 10.1175/JCLI-D-12-00556.1

the new generation of CGCMs provided by phase 5 of the Coupled Model Intercomparison Project (CMIP5) and assesses the model progress as compared with CMIP3.

The AWP develops in June, reaches its maximum during the four months of July–October (JASO), and decays quickly after October (Wang and Enfield 2003; Lee et al. 2007). For this annual cycle, Enfield and Lee (2005) showed that the AWP variation is largely forced by shortwave radiation while latent heat flux plays a secondary role, particularly during the AWP decay phase. This seasonal cycle in many of the CMIP3 models has a significant cold bias in the AWP region (Chang et al. 2007, 2008; Richter and Xie 2008; Misra et al. 2009; Richter et al. 2012; LWLE12). Large and Danabasoglu (2006) and Chang et al. (2007) both pointed out that the North Atlantic subtropical high and associated surface winds are stronger than observed. Grodsky et al. (2012) further examined the tropical Atlantic SST bias based on the Community Climate System Model, version 4 (CCSM4), and pointed out that the excess winds induced by erroneously high sea level pressure (SLP) cause excess surface latent heat loss and cold SST bias in the tropical North Atlantic (NTA). However, based on an analysis of observed air–sea fluxes, Misra et al. (2009) found that surface evaporation in the AWP region is weakly influenced by both surface winds and air–sea humidity variations, while in the National Centers for Environmental Prediction (NCEP) Climate Forecast System (CFS) the latent heat flux is only strongly modulated by the air–sea humidity variations. These studies indicate that, unlike in the NTA, increased winds and evaporation cannot fully explain the cold SST bias in the AWP region. Li and Xie (2012) summarized that the tropical SST bias can be classified into two types: one with the same sign across all basins, which is highly correlated with the tropical mean caused by biases in atmospheric simulations of cloud cover, and the other with large variability in the cold tongue regions caused by biases of oceanic thermocline depth. The AWP bias is more related to radiative flux errors due to local convection and clouds (LWLE12).

As the AWP is adjacent to the NTA and, in fact, includes the western NTA (the NTA is defined as the region of 5.5°–23.5°N, 57.5°–15°W), climate variability of the AWP is contemporaneously correlated with variability in the NTA to the east (Wang and Enfield 2003). Thus the major modes of the tropical Atlantic variability contribute to the AWP interannual and longer time scales. The correlations of the AWP with the tropical Atlantic meridional gradient mode (AMM) (Servain 1991; Chang et al. 1997, Xie et al. 1999; Enfield et al. 1999; Xie and Carton 2004) and the Atlantic Niño (Zebiak 1993; Carton and Huang 1994; Latif and Grötzner 2000; Okumura and Xie 2006) are statistically significant but relatively low compared with the correlations of the AWP with Niño-3 (5°S–5°N, 150°–90°W) SST anomalies and NTA SST anomalies, suggesting that the impacts of the AMM and the Atlantic Niño on the AWP are weaker than those of the Pacific El Niño and NTA (Wang and Enfield 2003). The different correlation of the AWP with AMM and NTA is consistent with the observation of Enfield et al. (1999) that the NTA and tropical South Atlantic are uncorrelated at zero lag and show different time scales of variability. Through rotated empirical orthogonal function (rEOF) statistical analysis, the southern tropical Atlantic (STA) pattern, NTA pattern, and subtropical South Atlantic (SSA) pattern are three major modes exhibited (Huang and Shukla 2005; Bates 2008). In CGCMs, however, the STA mode may demonstrate two separate patterns in the tropical South Atlantic. The mode with variability in the southern segment of the Benguela upwelling zone off the coast of Namibia is subcategorized as the STA-BG mode and the mode of the equatorial tongue pattern is subcategorized as the STA-EQ mode (Muñoz et al. 2012). The separation of STA-BG and STA-EQ in numerical models, unlike in the observations, is related to the model systematic bias of excessive southward shift of the intertropical convergence zone to around 10°S in boreal spring (Huang et al. 2004). An excessive southward shift of the Atlantic ITCZ in the CMIP3 model and its relation to the weak bias of the southerly wind along the African coast are also discussed by Richter and Xie (2008), Hu et al. (2008), and Doi et al. (2010). Tozuka et al. (2011) showed that the tropical Atlantic bias is highly sensitive to the choices of deep convection parameterization.

Another issue related to model performance and assessment is the extent to which the models reproduce the observed manner in which climate modes appear to force changes in the AWP. Much more of the NTA variability is caused by remote forcing from climate variability outside the tropical Atlantic than by the intrinsic self-sustained modes of the tropical Atlantic variability (Xie and Carton 2004). Czaja et al. (2002) showed that almost all NTA SST extreme events can be related to either ENSO or the NAO, consistent with Enfield et al. (2006). Analysis based on the National Oceanic and Atmospheric Administration (NOAA) Cooperative Institute for Research in Environmental Sciences (CIRES) Twentieth Century Global Reanalysis (20CR) indicates that both positive ENSO phase and the negative NAO phase in winter correspond to reduced trade winds in the AWP region (LWLE12). The westerly anomalies induced by positive ENSO and the negative NAO, associated also with increased sea level pressure and subsidence in the NTA, lead to local heating through

TABLE 1. The 19 models of CMIP5 involved in this study and their development institutions, letter denotations, short names used throughout the paper, and time periods of historical simulations. CMIP3 models are also listed by institutions for reference. (The letter A denotes observations.)

Institution	Letter denotation	Abbreviation	Historical run	CMIP3 model names defined in LWLE12
Canadian Centre for Climate Modeling and Analysis (CCCma), Canada	B	CanESM2	1850–2005	CGCMt47, CGCMt63
National Center for Atmospheric Research (NCAR), United States	C	NCAR CCSM4	1850–2005	CCSM3, Npcm1
Commonwealth Scientific and Industrial Research Organization (CSIRO), Australia, and Bureau of Meteorology (BOM), Australia	D	CSIRO Mk 3.6.0	1850–2005	CSIRO30, CSIRO35
Geophysical Fluid Dynamics Laboratory (GFDL), United States	E	GFDL CM3	1860–2005	GFDL20, GFDL21
	F	GFDL-ESM2G	1861–2005	
	G	GFDL-ESM2M	1861–2005	
National Aeronautics and Space Administration (NASA), Goddard Institute for Space Studies (GISS), United States	H	GISS-E2H	1850–2005	GISSaom, GISSer
	I	GISS-E2R	1850–2005	
Met Office Hadley Centre, United Kingdom	J	HadCM3	1859–2005	Uhadcm3, Uhadgem1
	K	HadGEM2-CC	1859–2005	
	L	HadGEM2-ES	1859–2005	
Institute for Numerical Mathematics (INM), Russia	M	INM-CM4	1850–2005	INMCM3
Institut Pierre Simon Laplace (IPSL), France	N	IPSL-CM5A-LR	1850–2005	IPSL
	O	IPSL-CM5A-MR	1850–2005	
	P	IPSL-CM5B-LR	1850–2005	
Max Planck Institute for Meteorology (MPI-M), Germany	Q	MPI-ESM-LR	1850–2005	MPI
	R	MPI-ESM-P	1850–2005	
Meteorological Research Institute (MRI), Japan	S	MRI-CGCM3	1850–2005	MRI
Norwegian Climate Centre, Norway	T	NorESM1-M	1850–2005	

reduced latent heat loss, ultimately leading to a warm SST during March–May (ENSO) and February–April (NAO). This behavior is a known feature of anomalous AWP growth and is well captured by only 5 models out of 22 CGCMs in CMIP3 (LWLE12).

The Atlantic multidecadal oscillation (AMO) (Delworth and Mann 2000; Enfield et al. 2001; Bell and Chelliah 2006) is an oscillatory mode occurring in the North Atlantic SST primarily on multidecadal time scales. Wang et al. (2008a) showed that the AWP variability coincides with the signal of the AMO—''the warm (cool) phases of the AMO correspond to more large (small) AWPs''—and suggested that the multidecadal influence of the AMO on Atlantic tropical cyclone activity (Goldenberg et al. 2001) may operate through the mechanism of the AWP-induced atmospheric changes. In CMIP3, the global SST difference pattern between large AWP years and small AWP years on the multidecadal time scale resembles the geographic pattern of the AMO for most coupled models (LWLE12).

Many studies have been conducted to evaluate the performance of CGCMs in the World Climate Research Program (WCRP) CMIP3 multimodel dataset (e.g., Saji et al. 2006; Joseph and Nigam 2006; Chang et al. 2007; Richter and Xie 2008; de Szoeke and Xie 2008; Wang et al. 2009). As the CMIP5 model dataset is now available, it is of interest to evaluate how well the new generation of CGCMs represents AWP variability in order to improve and apply coupled climate models for AWP research. In this study we analyzed 19 state-of-the-art CGCMs in the WCRP CMIP5 multimodel dataset as to how they replicate AWP variability from seasonal to multidecadal time scales as well as the AWP teleconnection with ENSO and the NAO. The remainder of the paper is organized as follows. The models, validation datasets, and methods used in this study are described in section 2. The AWP seasonal cycle and bias analysis are included in section 3. The AWP variability of interannual and longer time scales in CGCMs is studied and compared with observations and CMIP3 simulations in section 4. Section 5 summarizes the conclusions.

2. Data and methods

This study is based on output from historical simulations of 19 CGCMs in the WCRP CMIP5 multimodel dataset. The modeling center and country, CMIP5 model abbreviation and designated letter, and length of historical simulations for each model in this study are

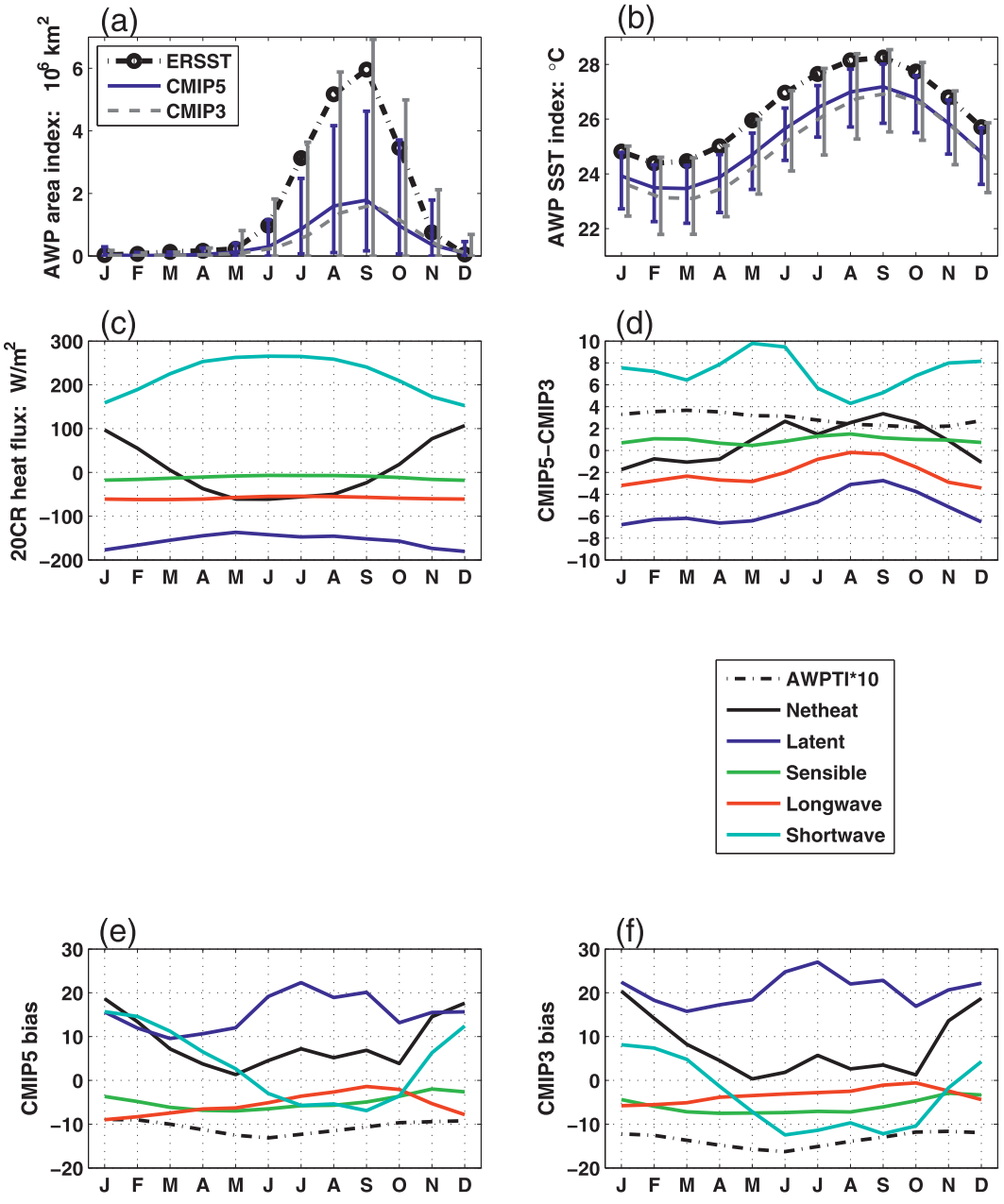

FIG. 1. Climatology of (a) AWPAI, (b) AWPTI (AWP box averaged), (c) net surface heat flux of 20CR, (d) net surface heat flux of CMIP5 minus CMIP3, (e) net surface heat flux of CMIP5 minus 20CR, and (f) net surface heat flux of CMIP3 minus 20CR. Positive value of heat fluxes mean ocean gains heat. AWP box is defined within 5°–30°N, land–40°W. Black line with circle is for ERSST in (a). Blue line is ensemble of CMIP5 CGCMs. Gray dashed line is the ensemble of CMIP3 models. Model spreads are represented by vertical bars. Black dashed lines in (d)–(f) stand for AWPTI × 10 (°C).

shown in Table 1. CMIP3 model abbreviations are also included for references in the table grouped by modeling center. The model data can be downloaded from the website of Program for Climate Model Diagnosis and Intercomparison (PCMDI; http://www-pcmdi.llnl.gov/). The historical simulations are spun up and then forced by solar, volcanic, sulfate aerosol, and greenhouse gas forcings (Meehl et al. 2007) from different starting years (1850, 1859, 1860, and 1861) to 2005.

Observational datasets are used to validate the variabilities of CGCM simulations. SST data are the NOAA Extended Reconstruction Sea Surface Temperature version 3 (ERSST) (Smith et al. 2008). The temporal coverage is from January 1854 to the present. (These data can be obtained from

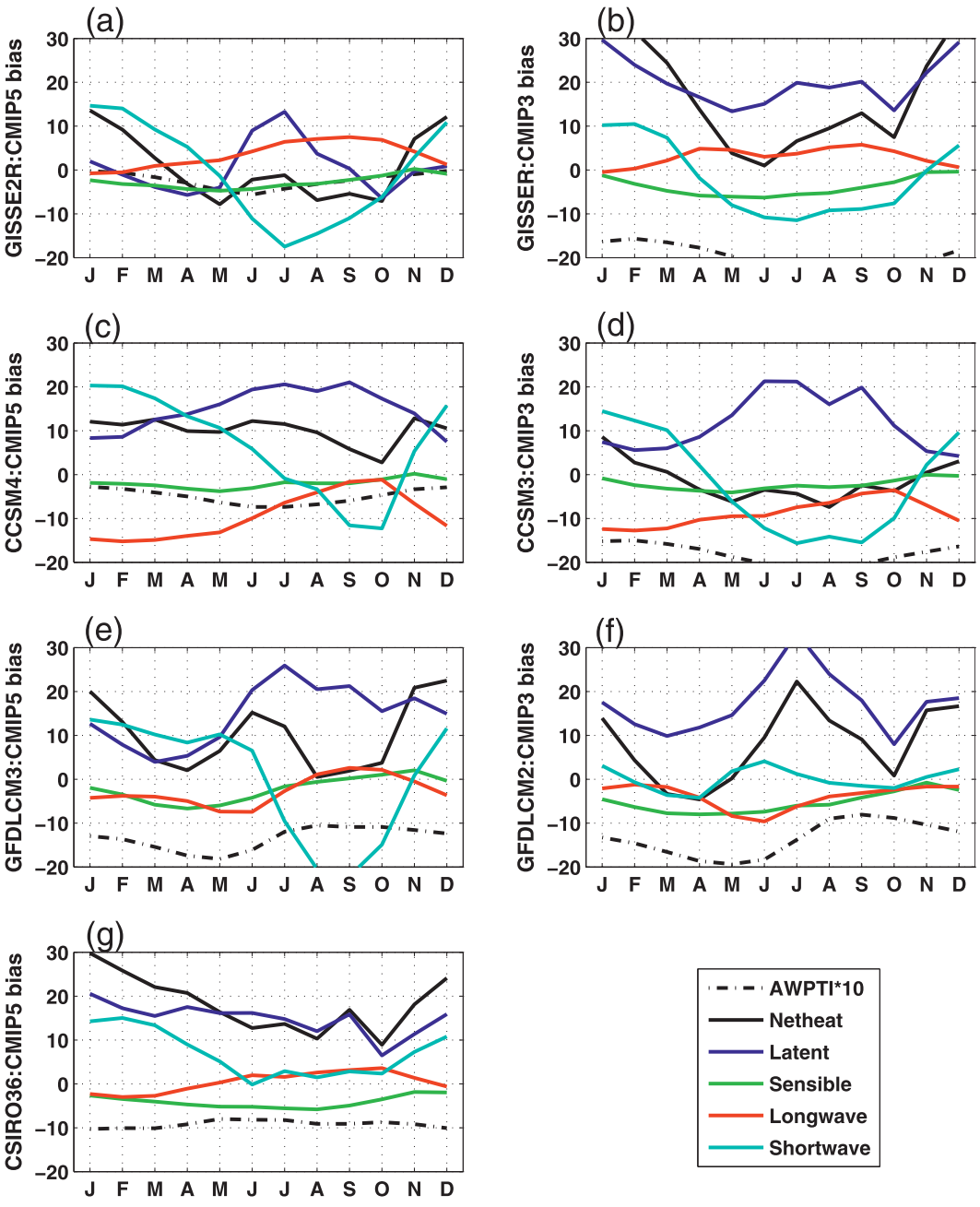

FIG. 2. AWP box averaged net surface heat flux bias (W m^{-2}) and AWPTI bias (°C) for selected models: (a) GISS-E2R (CMIP5), (b) GISS-ER (CMIP3), (c) CCSM4 (CMIP5), (d) CCSM3 (CMIP3), (e) GFDL CM3 (CMIP5), (f) GFDL CM2 (CMIP3), and (g) CSIRO Mk 3.6 (CMIP5).

http://www.ncdc.noaa.gov/oa/climate/research/sst/ersstv3.)php. Surface fluxes and SLP data are from NOAA–CIRES 20CR version II (Compo et al. 2011). This atmospheric reanalysis spans the entire twentieth century (1871–2008), assimilating only surface observations of synoptic pressure, monthly SST, and sea ice distribution. [More information about this dataset is provided at http://www.esrl.noaa.gov/psd/data/20thC_Rean/. Latent heat flux and surface winds from L'Institut Français de Recherche pour l'Exploitation de la Mer (IFREMER) are provided from ftp://ftp.ifremer.fr/ifremer/cersat/products/gridded/flux-merged (Bentamy et al. 2008).] This entire 16-yr (1992–2007) surface turbulent flux dataset estimated from satellite observations is improved from the previous version in assessing the surface winds from *European Remote Sensing Satellites 1* and *2* (*ERS-1* and

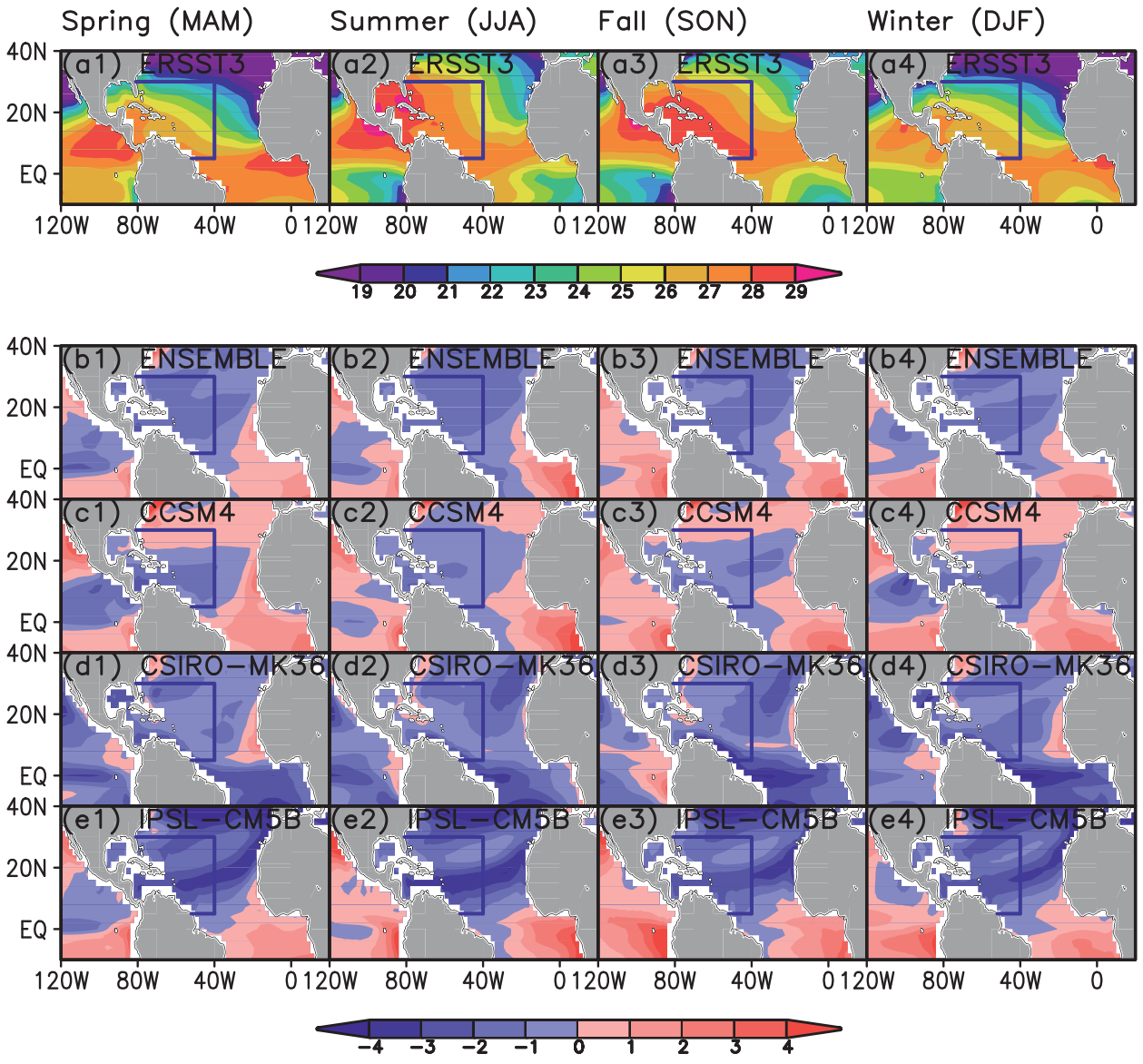

FIG. 3. Observational SST and model SST bias (°C) in four seasons: (a1)–(a4) ERSST averaged in four seasons, (b1)–(b4) the seasonal SST bias of the 19 model ensemble, and (c1)–(c4), (d1)–(d4), and (e1)–(e4) the seasonal SST bias for selected models.

ERS-2) and QuikSCAT scatterometers and using the new NOAA sea surface temperature estimates.

The AWP area index (AWPAI) is defined as the area inside the 28.5°C isotherm at the sea surface in the AWP region. Because of the cold SST bias in CGCMs the AWPAI cannot be defined for all the models and in certain years. So the AWP SST index (AWPTI) is defined in this study as the box-averaged SST from 5° to 30°N and the coast to 40°W. The Atlantic multidecadal oscillation (AMO) index is defined as the detrended area weighted average of the SST anomalies over the North Atlantic from 0° to 70°N (Enfield et al. 2001). The Niño-3 index is an average of the SST anomalies in the region 5°N–5°S, 150°–90°W. The NAO index is chosen as the difference of normalized SLP between 39°N, 9°W (Lisbon, Portugal) and 65°N, 22°W (Stykkisholmur/Reykjavik, Iceland) (Hurrell 1995). All indices are calculated for each model and observations. The clouds are classified by cloud-top height. The high-level clouds are 400 hPa or over, the middle-level clouds 400–600 hPa, and the low-level clouds 600 hPa or less as a rough standard. The cloud factions of the model outputs are integrated over these three layers separately to represent the low-level, middle-level, and high-level cloud amount.

Wavelet software for spectrum analysis was provided by C. Torrence and G. Compo (Torrence and Compo

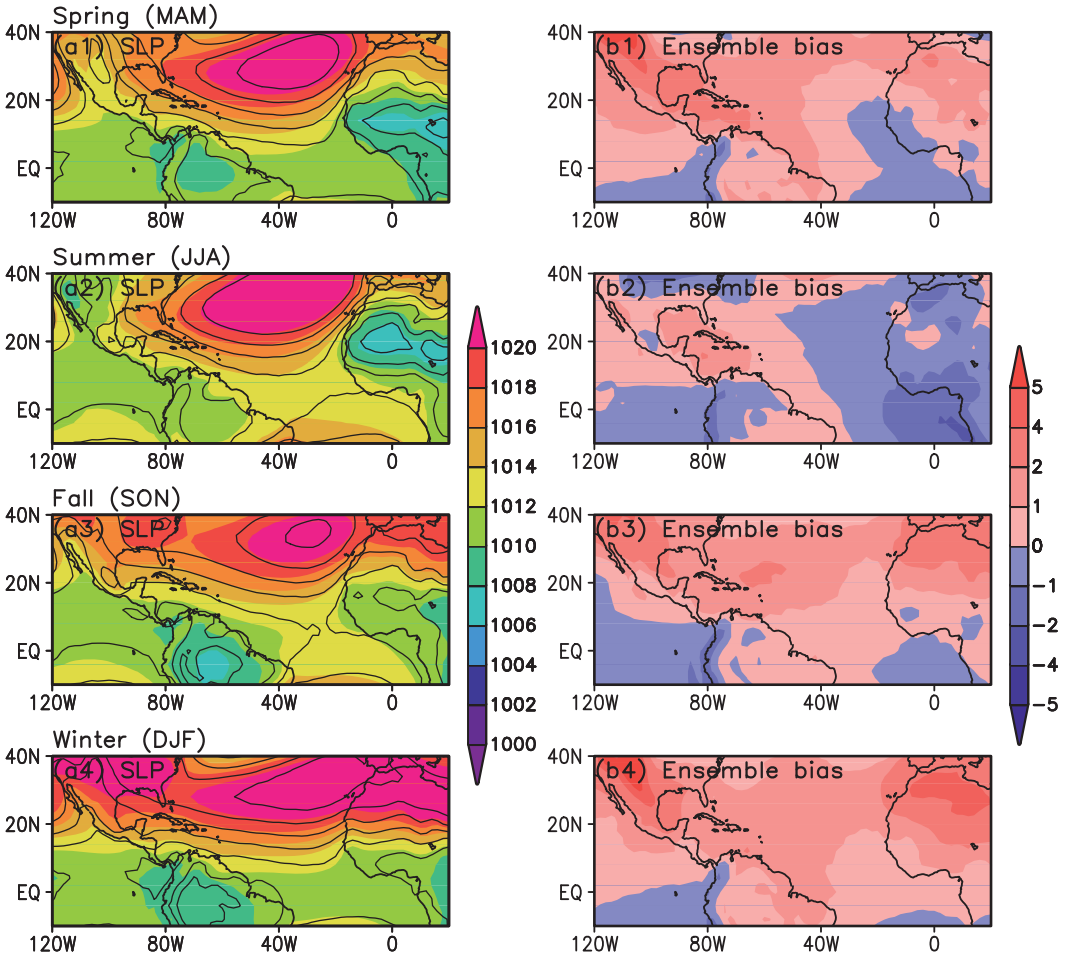

FIG. 4. Climatology of SLP (hPa) and model ensemble bias. (a1)–(a4) Climatology of SLP. Shading stands for model ensemble. Contour lines stand for 20CR. (b1)–(b4) Model ensemble bias for four seasons compared with 20CR.

1998) for spectrum analysis. The Taylor diagram (Taylor 2001) is applied to quantify how well models simulate an observed climate field. It relies on three nondimensional statistics: 1) the ratio of the variances of the two fields (r, which is the standard deviation of the model divided by standard deviation of the observations); 2) the correlation between the two fields (R, which is computed after removing the overall means); and 3) the root-mean-square error between models and observation (E, which is normalized by the standard deviation of the observed field). This diagram provides a 2D graph based on the three statistics summarizing how closely a pattern matches observations.

3. AWP climatology

a. Seasonal cycle

The AWPAI of the 19-model ensemble [note that in this study models (CGCMs) indicate the models from CMIP5 or general meaning unless CMIP3 follows] is slightly increased during July–September (JAS) compared with the ensemble of AWPAI in CMIP3 (Fig. 1a). Although the seasonal cycle of AWPAI ensemble with peaks in JASO is well simulated, it is still much underestimated compared with ERSST due to the cold SST bias in the AWP region (Misra et al. 2009; LWLE12). The bias of APWAI reaches -4.2×10^6 km^2 in summer, but almost no bias exists in January as there is no AWP in winter based on the definition. The spread of the models' AWPAI contracts in contrast with the spread of CMIP3. The AWPAI of 10 models is less than 20% of ERSST AWPAI in summer and for some certain years AWPAI of a part of CGCMs cannot be computed to study their interannual and multidecadal variability due to the cold SST bias. Therefore, the AWPTI is used for this study.

Figure 1b shows the AWPTI of the model ensemble mean successfully representing the seasonal cycle of ERSST, which peaks in JASO. However, there is cold bias throughout the year with a minimum cold bias of

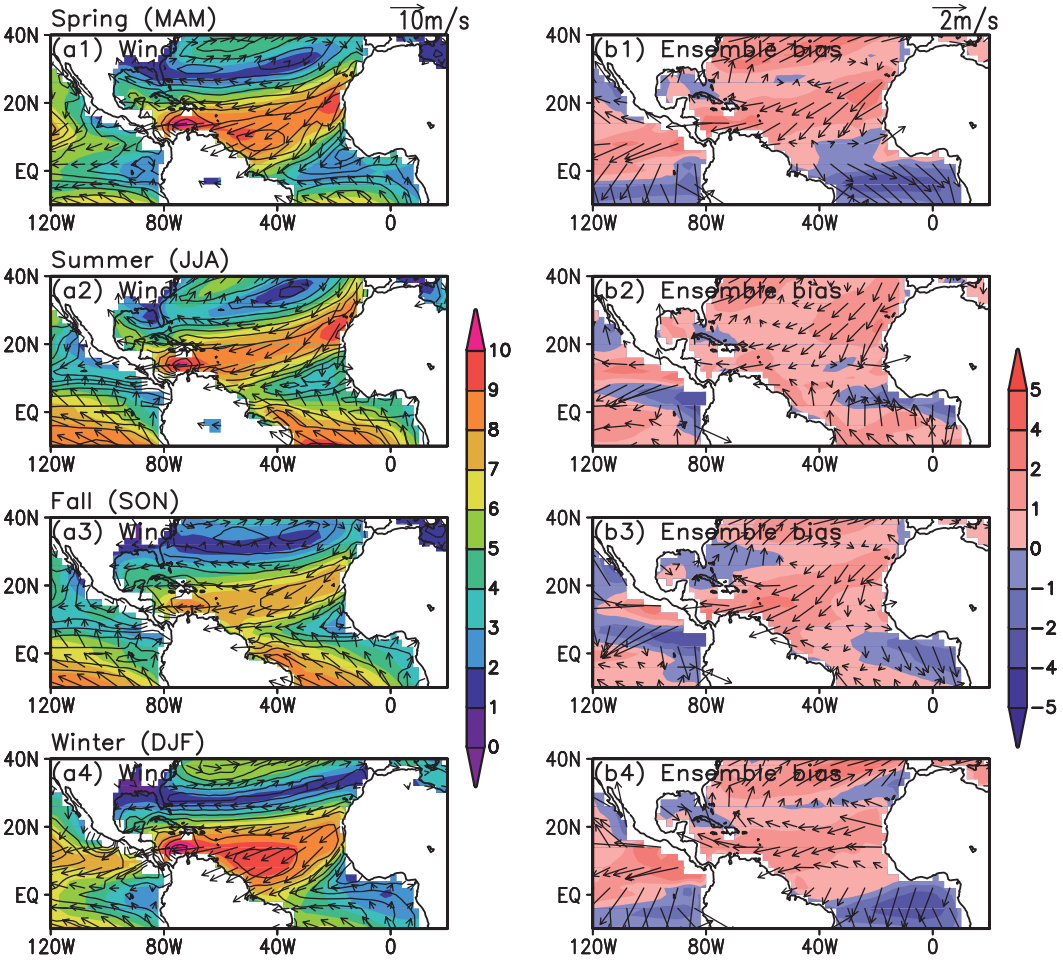

FIG. 5. Climatology of surface winds (m s^{-1}) and model ensemble bias. (a1)–(a4) Climatology of surface winds. Shading stands for wind speed of model ensemble. Vectors stand for wind vectors of model ensemble. Contour lines stand for wind speed of IFREMER data. (b1)–(b4) Model ensemble bias for four seasons compared with IFREMER data. Shading stands for wind speed bias and vectors stand for wind vector bias.

0.89°C in January and maximum cold bias over 1.2°C in May–July (MJJ). The spread is consistent for all months with a range of 1.9°–2.2°C. Compared with CMIP3, the ensemble mean of AWPTI increases about 0.3°C all year round (Fig. 1d), and the spread of models also contracts about 1°C. To some extent the performance of CMIP5 in simulating AWP seasonal cycle is improved from the view of the model ensemble. The improvement of model ensemble mean may be explained by the slight increase of net surface heat flux in CMIP5 (Fig. 1d). Compared with CMIP3, the ensemble mean of net surface heat flux increases within a range of 1.5–3.4 W m^{-2} during June–October (JJASO). This increase accounts for ~0.1°C temperature change if we roughly estimate the mixed layer depth at about 25 m in the AWP region. For each component of surface heat fluxes, the ensemble mean of CMIP5 has more latent heat loss (heat loss means that ocean loses heat; heat gain means that ocean gains heat), more longwave radiation loss, less sensible heat loss, and more net shortwave radiation gain (Fig. 1d) compared with CMIP3. However, the ensemble mean in both CMIP3 (Fig. 1f) and CMIP5 (Fig. 1e) possesses the same sign of bias for each component of surface heat fluxes except net shortwave radiation given the reference of 20CR. Wang and Enfield (2001) suggested that the SST seasonal variations in the AWP region are induced primarily by surface net heat flux with a phase lag of 3–4 months. The shortwave and latent heat fluxes are the two largest terms. The shortwave flux has a maximum value from April to August, and the latent and sensible heat losses have their minima around May owing to lower winds speeds associated with the seasonal south–north movement of the ITCZ. Minimum longwave radiation occurs from July to September because greater cloud cover results in an increase in the downward longwave radiation from cloud ceilings. This results in

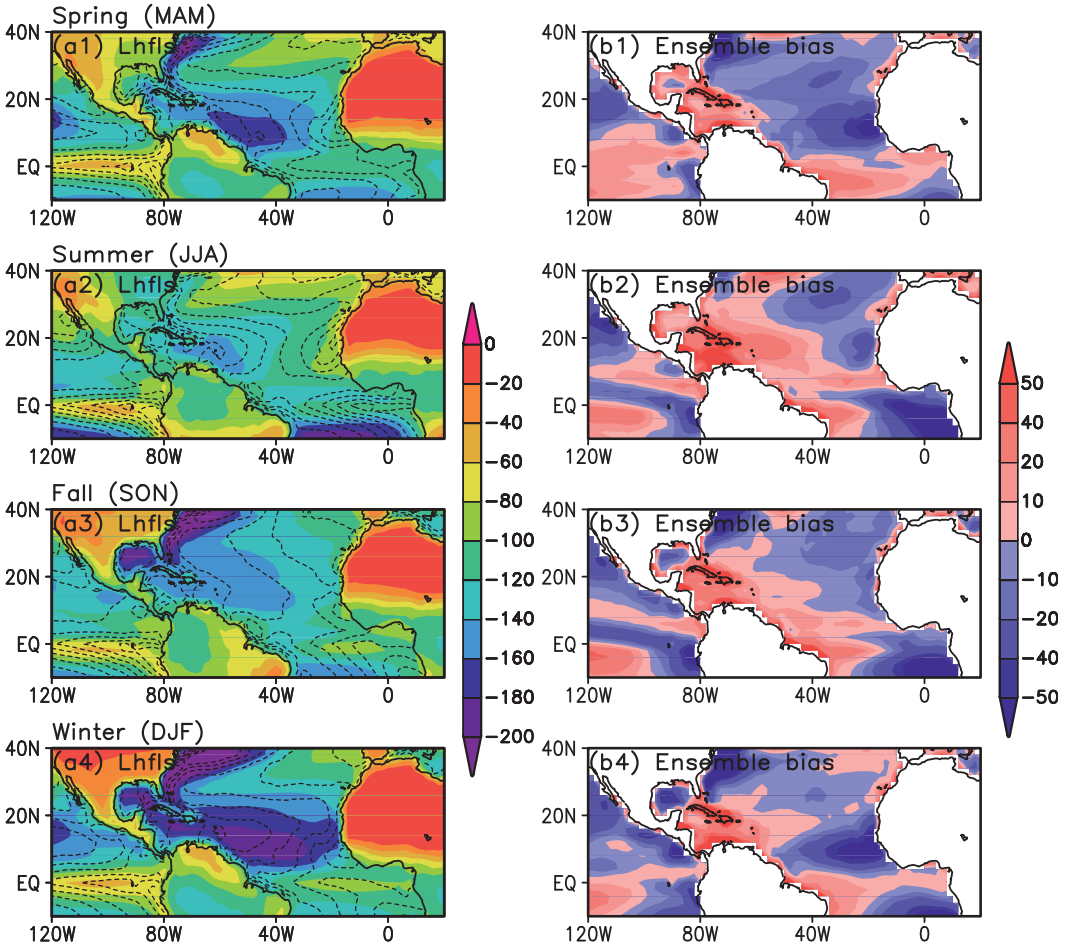

FIG. 6. Climatology of latent heat flux (W m^{-2}) and model ensemble bias. (a1)–(a4) Climatology of latent heat flux. Shading stands for model ensemble. Contour lines stand for IFREMER data. (b1)–(b4) Model ensemble bias for four seasons compared with IFREMER data.

the maximum of net heat flux occurring in late spring and maximum SST in fall. These relationships between heat fluxes and AWP SST are well reflected in the 20CR (Fig. 1c), CMIP3, and CMIP5 ensemble mean.

We categorize the CMIP5 models into different groups based on their development institutions. For the group of GISS models (see the appendix for a complete list of the institutional models), both GISS-E2H and GISS-E2R have better performance in simulating the AWP seasonal cycle compared with previous generation of GISS-AOM and -ER. The AWPTI bias of GISS-E2R (Fig. 2a) is much smaller than the GISS-ER (Fig. 2b). Compared with GISS-ER, the latent heat flux bias decreases most in GISS-E2R. However, this decreased positive latent heat flux bias is not able to explain the decreased negative AWPTI bias. For the NCAR group, CCSM4 (Fig. 2c) is much improved from CCSM3 (Fig. 2d) for the seasonal AWPTI simulation. Compared with CCSM3 for each component bias of surface heat fluxes, the shortwave heat flux bias changes the most in CCSM4. This increased shortwave heat flux in CCSM4 may explain the decreased negative AWPTI bias. Both GISS-E2R and CCSM4 improve the simulation of AWPTI from the corresponding last generation CGCMs, but the heat flux component bias analysis cannot give a consistent conclusion why the simulations are improved.

For the GFDL group, GFDL CM3 (Fig. 2e), GFDL-ESM2G, and GFDL-ESM2M (not shown) of CMIP5 have no better performance in simulating the AWP seasonal cycle compared with GFDL CM2 (Fig. 2f) of CMIP3. The CM3 has a notable difference in seasonal cycle of surface heat fluxes compared with the other GFDL models. In summer, CM3 has less sensible heat loss, less longwave radiation loss, and shortwave radiation gain, with the net heat flux peaking one month earlier than the other GFDL models (Figs. 2e,f).

For the CSIRO group, the CSIRO Mk 3.6 (Fig. 2g) of CMIP5 has larger AWPTI negative bias but also has

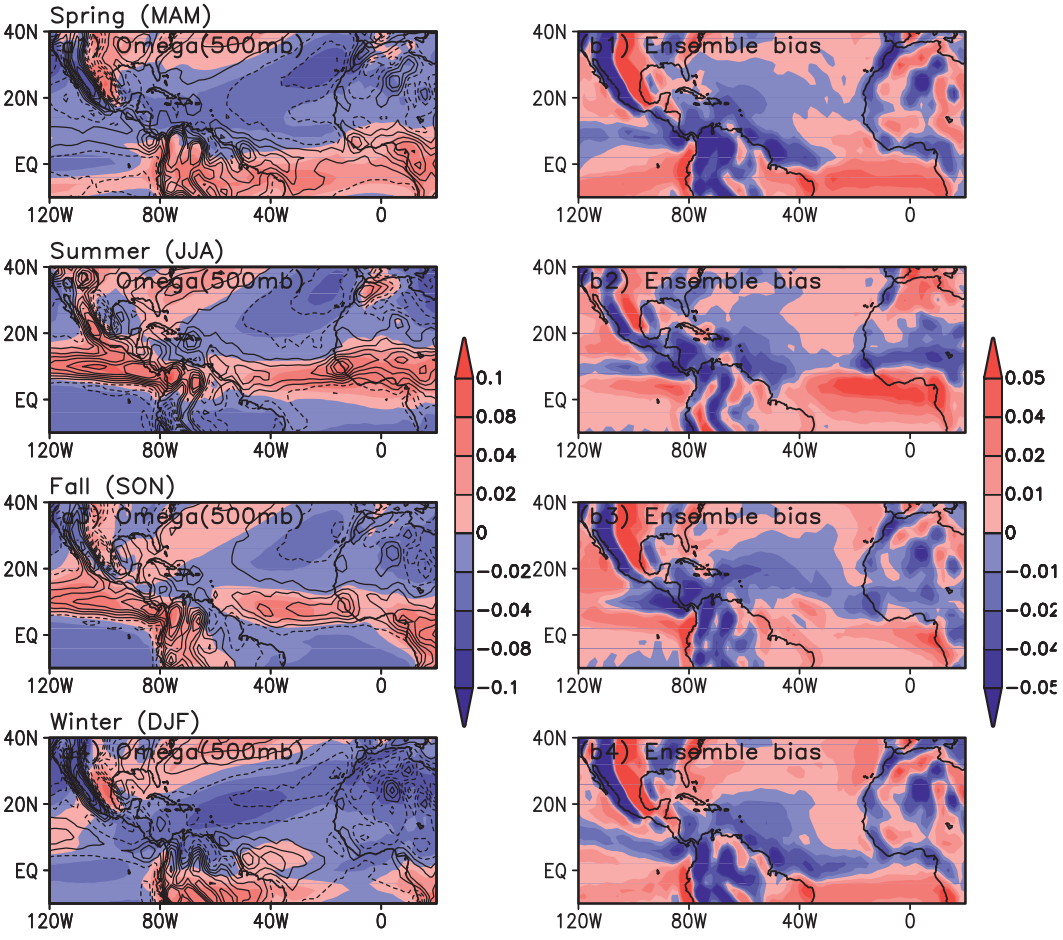

FIG. 7. Climatology of pressure vertical velocity (Pa s^{-1}) and model ensemble bias. (a1)–(a4) Climatology of pressure vertical velocity. Shading stands for model ensemble. Contour lines stand for 20CR. (b1)–(b4) Model ensemble bias for four seasons compared with 20CR. The sign of pressure vertical velocity is reversed and subsidence corresponds to negative pressure velocity.

larger positive net heat flux compared with CSIRO Mk 3.5 of CMIP3 (not shown). The larger net heat flux of CSIRO Mk 3.6 is not able to explain the weaker amplitude of AWPTI compared with Mk 3.5, which may indicate that oceanic processes play a role.

For the other groups of CGCMs, detailed discussions are not included. In general there are no unanimous conclusions as to how the surface fluxes components affect the AWPTI bias. But, for some models, such as the GFDL CM3 (Fig. 2e) and CM2 (Fig. 2f) and CSIRO Mk 3.6 (Fig. 2g), the seasonal cycle of longwave radiation bias is highly correlated with AWPTI bias; also, for some models, such as GISS-ER (Fig. 2b) and CCSM3 (Fig. 2d), the seasonal cycle of shortwave radiation bias is correlated with AWPTI bias. Thus AWP SST bias in the CGCMs possibly relates to different physical mechanisms associated with shortwave and longwave radiation.

In summary, the AWP (AWPAI and AWPTI) seasonal cycles of NCAR CCSM4, CSIRO Mk 3.6.0, GISS-E2H, GISS-E2R, HadCM3, MPI-ESM-LR, and MPI-ESM-P have amplitudes comparable to those of ERSST. Although each individual model has changed or made no progress in simulating the AWP seasonal cycle compared with its corresponding previous generation model, the ensemble mean of AWP climatology in CMIP5 models is somewhat improved overall, and the model ensemble spread has decreased. However, the state-of-the-art CGCMs in CMIP5 still suffer from a significant cold bias in the AWP region.

b. Bias analysis

The AWP peaks in summer and fall. To compare with ERSST, the SST bias pattern is shown for the 19-member ensemble mean of CMIP5 (Figs. 3b1–b4) and for selected models (Figs. 3c–e). The ensemble mean character similar with CMIP3 (LWLE12) as shown in Figs. 3b1–b4 is that, in addition to the cold bias north of the equator, the southeast Atlantic warm SST bias including the cold

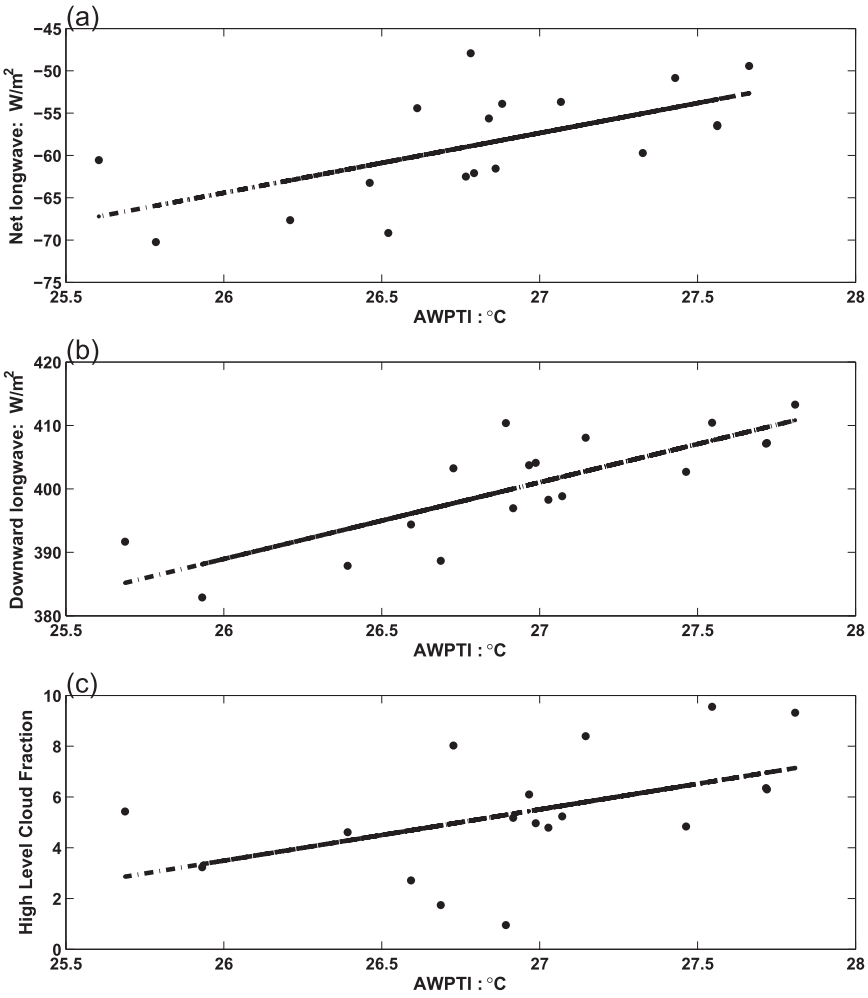

FIG. 8. Multimodel scatterplot in JASO of (a) net longwave radiation vs AWPTI, (b) downward longwave radiation vs AWPTI, and (c) high-level cloud fraction vs AWPTI. Each point stands for one model. The black line shows the least squares linear fit to all points.

tongue and the Angola–Benguela coastal regions exists in all the models except CSIRO Mk 3.6 (Figs. 3d1–d4) for all four seasons. It is possible that the positive feedback of wind, evaporation, and SST (WES), which causes the tropical Atlantic variability (Xie and Carton 2004), may generate these opposite biases across the equator. The process is that the warm bias in the southeast tropical Atlantic induces stronger northeast trade winds in the tropical North Atlantic (NTA), and then leads to more latent heat loss; therefore, a cold SST bias of the NTA can be formed, which in turn decreases the southeast trade winds and enhances the warm bias in the southeast tropical Atlantic due to less latent heat loss. IPSL-CM5B-LR (Figs. 3e1–e4), similar to IPSL-CM5A-LR, IPSL-CM5A-MR, and MRI-CGCM3 (not shown), has a cold bias with maxima across the tropical North Atlantic, which resembles a strip and is located near 15°N. This character is different from the cold SST bias pattern of the NTA in the other CGCMs, which indicates that different mechanisms lead to the cold bias in the CGCMs.

Grodsky et al. (2012) found that the atmospheric component of CCSM4 has abnormally intense surface subtropical high pressure systems, which cause the northeast trade winds to be too strong and lead to an excessively large latent heat loss in the NTA region. Before we examine this process here for the CMIP5 CGCMs, it should be noted that the cold SST bias enhances the SLP by raising the air density above it. In fact, the positive (negative) SLP bias (right panels in Figs. 4b1–b4) is largely collocated with the cold (warm) SST bias (Figs. 3b1–b4), which seems to support a strong effect (or feedback) of the SST bias on the SLP. Except for GISS-E2H, GISS-E2R, and HadCM3, the SLP bias pattern of

16 of the CGCMs shares the similarity with the ensemble as shown in Fig. 4. The CGCMs can capture the major characters of SLP climatology (Figs. 4a1–a4), but in most of the NTA region the CGCMs overestimate SLP by 2 hPa (Figs. 4b1–b4). In the northeast trade winds region of the CGCM ensemble (Figs. 5a1–a4), there is always a positive wind speed bias throughout all four seasons (Figs. 5b1–b4). The latent heat loss maximum centered to the south of the Gulf Stream is mainly located in the AWP region (Figs. 6a1–a4). The latent heat loss bias in the AWP region is positive instead of negative as shown in the NTA region for the CGCM ensemble (Fig. 6b). It suggests that for most models, the NTA cold SST bias can be traced to excessive evaporation due to erroneously high SLP and strong northeast trade winds. However, in the AWP region this mechanism is not able to explain the cold SST bias.

The pressure vertical velocity at 500 mb of the CGCM ensemble (Figs. 7a1–a4) shows the location of the ITCZ and its seasonal cycle. Compared with 20CR, the CGCMs have subsidence bias in the AWP region all year round. This subsidence bias may be induced by overturning through the uplift process in the ITCZ of the east Pacific (Figs. 7b1–b4) since convection over the Amazonian region is also much weakened in CGCMs. The subsidence bias tends to suppress high-level cloud formation and increase low-level cloud formation. LWLE12 found that the negative SST bias of CMIP3 in the AWP region is connected with an excessive amount of simulated low-level cloud, which blocks shortwave radiation from reaching the sea surface. This positive feedback of colder SST, increased fraction of low level cloud, and decreased surface shortwave flux (Fig. 9) may enhance the cold SST bias. However, it is uncertain to what extent the excessive simulated low-level clouds in CMIP3 CGCMs cause, or are caused by, the SST bias. The same analysis was performed on the output from CMIP5 CGCMs. We do not find the relationship of higher AWP SST corresponding to more shortwave radiation and less low-level cloud fraction during the AWP peak season. Higher AWP SST in August–October (ASO), however, corresponds to less net longwave heat loss (Fig. 8a), due to an increase in the downward longwave heat flux (Fig. 8b) and to more high-level cloud fraction among the CMIP5 CGCMs. This relationship suggests that, although there is still subsidence bias for the CMIP5 CGCMs in the AWP region, excessive high-level clouds are simulated (Jiang et al. 2012) and the warming effect of the high-level clouds radiative forcing (Su et al. 2008), as shown in Fig. 9, dominates the modulation of AWP SST bias (the warming effect of the high-level clouds means that high-level clouds tend to reflect more longwave radiation back to the earth's surface and have less impact on downward shortwave radiation and, therefore, have a warming effect on sea surface). Thus, more (less) high-level cloud simulation may decrease (enhance) the cold AWP SST bias.

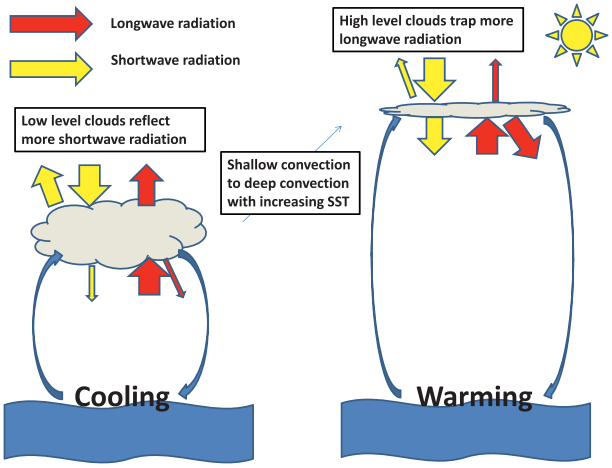

FIG. 9. Diagram of different radiative properties of low- and high-level clouds and their associated feedback with SST in the AWP region.

Why are excessive high-level clouds simulated compared with CMIP3? Significant improvement in both deep and shallow convection schemes have been made in CMIP5. For example, GFDL AM3, the atmospheric component of CM3 (Donner et al. 2011), includes new treatment of deep and shallow cumulus convection, cloud droplet activation by aerosols, subgrid variability of stratiform vertical velocities for droplet activation, and atmospheric chemistry driven by emissions with advective, convective, and turbulent transport. The other possible reason is that the mean state of AWP SST of CGCMs increases in CMIP5 although the cold SST bias still exists. In general, lower SST tends to form more shallow convection and leads to more convection-related low-level clouds. Higher SST tends to induce more deep convection and then more high level clouds can be formed. The increases of mean AWP SST in CMIP5 may also mitigate the excess low-level cloud formation and explain why low-level clouds and AWPTI are not correlated in CMIP5. Again the ultimate origin of the cold bias remains unknown.

4. AWP variability

a. Spectrum analysis

Power spectrum analyses of the time series of monthly AWPTI are shown in Fig. 10. There is significant energy at multidecadal periods between about 20 and 32 yr and longer than 32 yr in ERSST (Fig. 10a). The spectrums

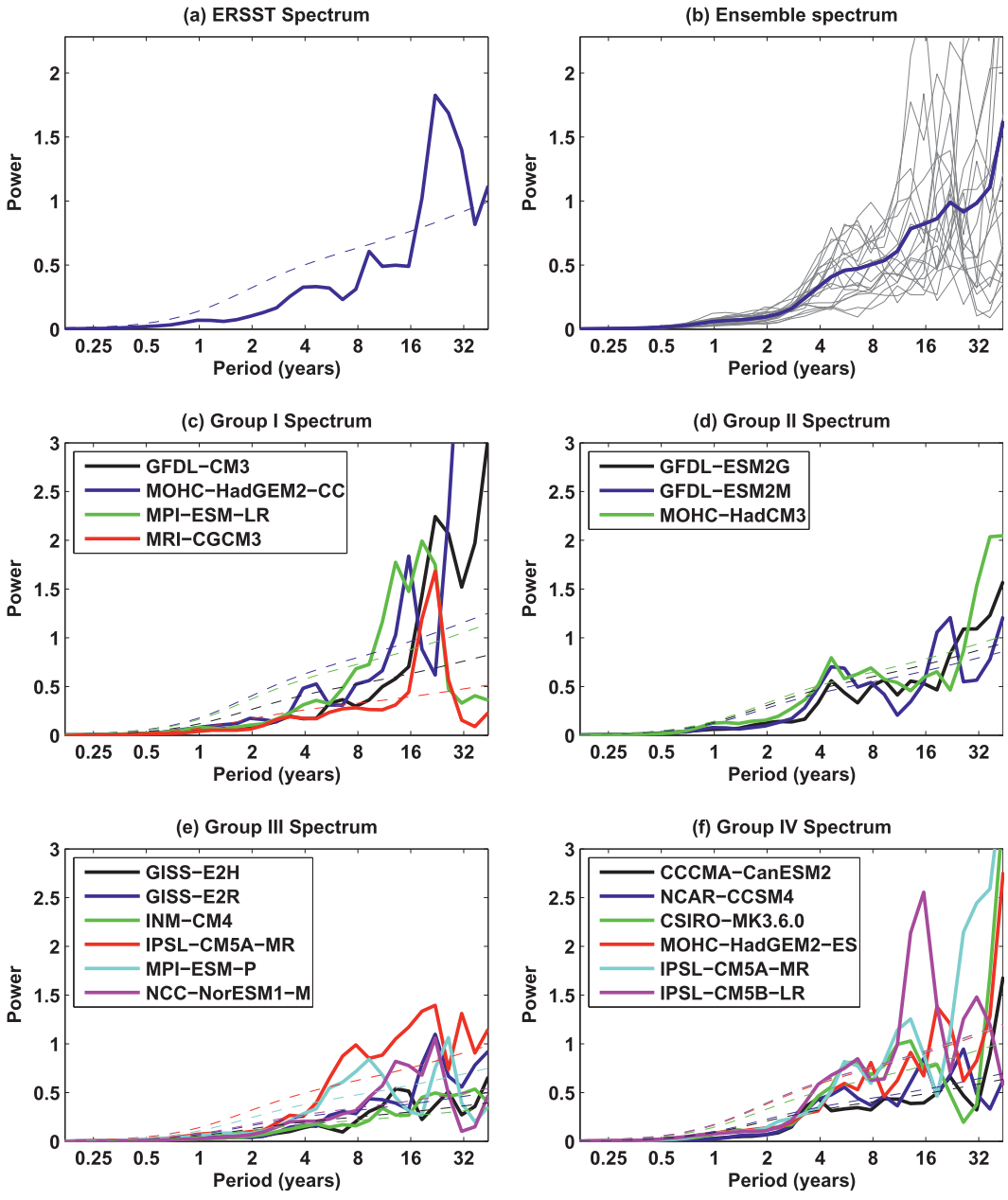

FIG. 10. Spectrum analysis of AWPTI. (a) Spectrum of ERSST. The *y* axis is power and the *x* axis is the wavelet period in years. The dashed line indicates 95% significance level. (b)–(e) As in (a), but for the ensemble of 19 models with each model shown as a gray line, for Group I, II, III, and VI models, respectively.

of most CGCMs, however, demonstrate peaks in the interannual band (3–7 yr), the decadal band (8–20 yr), and the multidecadal band (20–30 yr, 40–60 yr, or longer), all with 95% significance as shown in Fig. 10b. The ensemble spectra of the CGCMs also reflect the three bands. Based on the spectral character of the model ensemble, four groups of models are categorized as shown in Table 2. In category I (as shown in Fig. 10c), four models simulate the significant multidecadal bands: GFDL CM3, HadGEM2-CC, MPI-ESM-LR, and MRI-CGCM3. In category II (shown in Fig. 10d), three models simulate the interannual band and multidecadal bands: GFDL-ESM2G, GFDL-ESM2M, and HadCM3 at the 95% significance level. In category III six models (Fig. 10e), consisting of GISS-E2H, GISS-E2R, INM-CM4, IPSL-CM5A-MR, MPI-ESM-P, and NorESM1-M, simulate significant variability for the decadal and multidecadal bands. In category IV six models simulate significant

TABLE 2. First four rEOF modes of ERSST and CGCMs with their variances. Abbreviations are STA: southern tropical Atlantic mode; NTA: northern tropical Atlantic mode; SSA: subtropical South Atlantic mode; STA-EQ: equatorial component of southern tropical Atlantic mode; STA-BG: Benguela component of southern tropical Atlantic mode; and NTA II: the second mode of NTA caused by model bias. (Models marked with an asterisk are identified as the category I group in the text.)

Observations and models	rEOF1	rEOF2	rEOF3	rEOF4
ERSST	STA-EQ: 17.0	NTA: 13.0	STA-BG: 10.3	SSA: 10.2
CanESM2	SSA: 20.0	NTA: 14.1	STA: 13.3	NTAII: 9.7
NCAR CCSM4*	STA-EQ: 24.4	SSA: 12.4	STA-BG: 10.1	NTA: 10.0
CSIRO Mk 3.6.0	NTAII: 21.3	NTA: 15.3	SSA: 13.5	STA: 11.0
GFDL CM3	STA: 34.4	NTA: 10.7	—: 9.0	—: 8.5
GFDL-ESM2G	STA: 20.6	NTA: 13.6	NTAII: 10.1	—: 10.1
GFDL-ESM2M	STA-EQ: 35.4	—: 13.0	NTA: 9.6	STA-BG: 6.7
GISS-E2H*	STA-BG: 20.6	NTA: 15.6	STA-EQ: 13.9	SSA: 8.6
GISS-E2R	STA-BG: 20.0	NTAII: 12.4	NTA: 11.2	SSA: 10.9
HadCM3	NTA: 15.9	—: 14.3	NTAII: 13.2	STA: 12.1
HadGEM2-CC	NTA: 19.3	STA: 19.2	—: 8.6	—: 7.5
HadGEM2-ES	NTA: 20.6	STA: 18.4	—: 8.1	SSA: 4.9
INM-CM4	STA: 15.4	NTA: 11.2	SSA: 8.8	—: 7.4
IPSL-CM5A-LR	NTA: 22.4	STA: 20.5	NTAII: 13.7	SSA: 12.3
IPSL-CM5A-MR	NTA: 24.2	STA: 17.0	SSA: 13.3	NTAII: 10.3
IPSL-CM5B-LR	NTA: 41.8	NTAII: 9.9	STA: 9.2	SSA: 5.7
MPI-ESM-LR	STA: 17.4	—: 17.3	NTA: 13.0	NTAII: 7.9
MPI-ESM-P	STA: 19.4	NTA: 11.7	—: 10.8	NTAII: 6.9
MRI-CGCM3	NTAII: 15.9	STA: 13.5	NTA: 10.7	SSA: 6.8
NorESM1-M	STA-EQ: 27.5	—: 14.9	STA-BG: 10.2	NTAII: 8.5

variability for the interannual, decadal, and multidecadal bands (Fig. 10f): CanESM2, NCAR CCSM4, CSIRO Mk 3.6.0, HadGEM2-ES, IPSL-CM5A-MR, and IPSL-CM5B-LR. Because a higher SST anomaly leads to increase deep convection and the convection-related net heat flux tends to cool the AWP (Wu et al. 2006), this local air–sea interaction tends to damp AWP SST anomalies and decrease their interannual variability, although the AWP still demonstrates substantial interannual variations through nonconvection-related processes such as advection. However, no significant periods are shown for the AWP interannual variability of the observations. The CGCMs are limited in their representation of the local air–sea interaction as discussed in Wu et al. (2006) and also show strong AWP internal variability with significant periods on the interannual band (LWLE12). The source of low-frequency variability on the multidecadal time scale is possibly from oceanic processes (Delworth and Mann 2000).

In summary, spectrum analysis of ERSST reveals that multidecadal variability is dominant in the AWP region. It suggests that there is no significant period for interannual variability. It does not mean that the interannual variation is weak. On the contrary, the standard deviation of AWPTI on the interannual band for both observation and CGCMs is larger than the deviation on the longer time scales (Fig. 11). Eleven out of 19 CGCMs have larger standard deviation of AWPTI compared with observations. In the next two sections, we focus on the interannual and multidecadal variability of the AWP in its peak season.

b. Interannual variability

We perform rEOF analysis on the tropical Atlantic ASO SST from 30°S to 30°N, as shown in Fig. 10. The first mode of observations with 17.0% variance (Fig. 12a1) is an STA-EQ mode featuring maximum SST anomalies on the equator and associated changes in the easterly trade winds (Philander 1986; Zebiak 1993; Carton and Huang 1994). The second mode is the NTA mode with 13.0% variance (Fig. 12a2). The SST anomalies are centered near the African coast in the northern tropical Atlantic Ocean. The third mode is the STA-BQ mode with 10.3% variance, characterized by SST fluctuations centered along the Benguela coast. The fourth mode is SSA mode with 10.2% variance, featuring maximum SST anomalies in the open ocean of the subtropical Atlantic. AWP interannual variability is primarily dominated by these four modes although the variance of these modes in the AWP region is small.

The rEOF modes of CGCMs are listed in Table 2. Compared with the rEOF modes of ERSST, the CGCMs are categorized into three groups. Category I, consisting of NCAR CCSM4 (Figs. 12b1–b4) and GISS-E2H (Figs. 12c1–c4), successfully captures all of the first four modes of observations with the overall character of each mode. Category II, consisting of CanESM2, CSIRO Mk 3.6.0, GISS-E2R, HadGEM2-ES, INM-CM4,

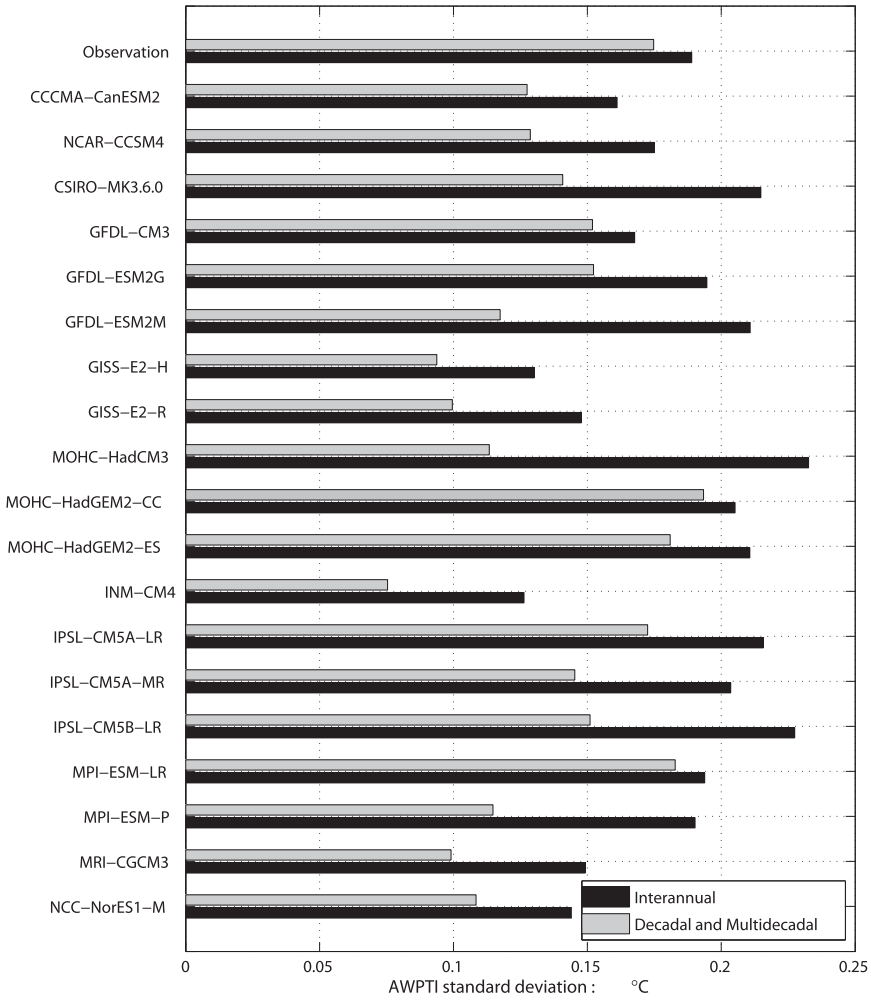

FIG. 11. AWPTI standard deviation of observations and CGCMs: interannual (black bar) decadal and longer time scale (gray bar).

IPSL-CM5A-LR, IPSL-CM5A-MR, IPSL-CM5B-LR, and MRI-CGCM3 (Figs. 12d1–d4), is able to simulate the SSA, NTA, and STA in their first four modes. In this group the CGCMs, however, cannot separate STA-EQ and STA-BG modes. A different type of NTA mode across the basin, as shown in Fig. 12d1, is captured by many CMIP5 CGCMs, and we defined it as the NTA II mode. Huang et al. (2004) pointed out that this mode is likely stronger in boreal summer in the tropical Atlantic and seems to be associated with the tropical extension of midlatitude SST anomalies as the ''North Atlantic horseshoe'' pattern. This pattern also resembles the remote forced pattern in NTA by ENSO and the NAO (Czaja and Marshall 2001). As the remote connection is discussed in section 4d, we find that for some CGCMs the influences of the NAO and/or ENSO can last from boreal spring to summer (as shown in Figs. 14e1 and 14e2). This overestimated remote forced pattern in summer can be embedded in tropical Atlantic variability, and here we ascribe remote forcing to the cause of the NTA II mode of CGCMs. Category III, consisting of GFDL CM3, GFDL-ESM2G, GFDL-ESM2M, HadCM3, HadGEM2, MPI-ESM-LR, MPI-ESM-P, and NorESM1-M, can only capture two modes of the first four ERSST modes. The patterns that cannot be defined as any one of the four modes of ERSST are not discussed but are listed in Table 2. Those patterns may be related with model bias.

c. *Multidecadal variability*

Based on the AWPTI of ERSST, the pattern of global SST difference between large AWP years and small AWP years on the multidecadal time scale is shown in Fig. 13a. The threshold value of AWPTI to define large (small) AWP years is 0.1°C (−0.1°C). As discussed by LWLE12, this pattern is identical to the pattern regressed on AWPAI of JJASO (Wang et al. 2008a) but also

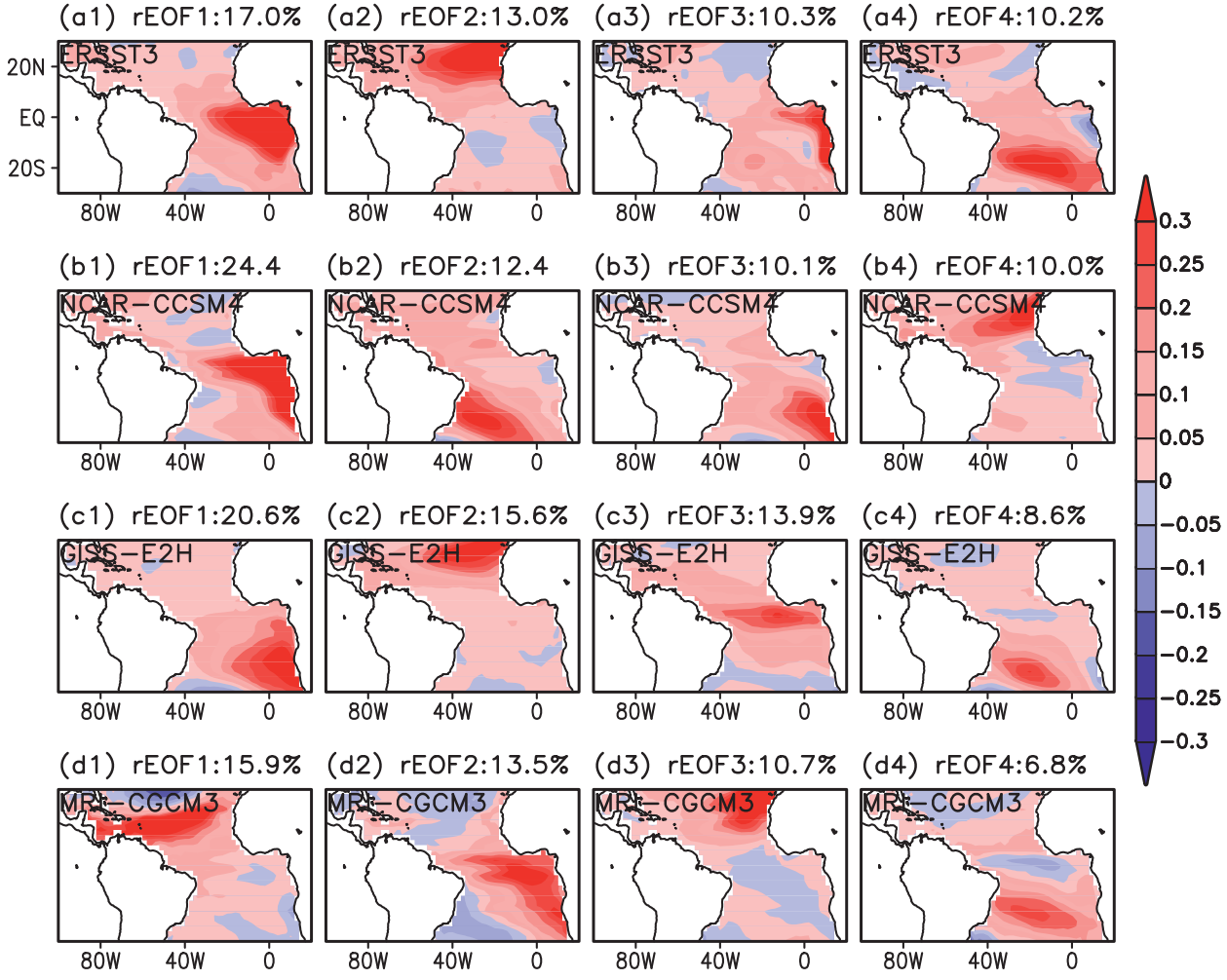

FIG. 12. The rEOF analysis of tropical Atlantic SST in ASO months: (a1) first, (a2) second, (a3) third, and (a4) fourth modes of ERSST. (b)–(d) As in (a), but for (b1)–(b4) NCAR CCSM4, (c1)–(c4) GISS-E2H, and (d1)–(d4) MRI-CGCM3.

has a global warming signature included because the linear detrending cannot remove the entire global warming signal. The spatial pattern suggests that the AWP multidecadal variability resembles the AMO, which is well supported by a close relationship between the AWPTI and AMO index. For the ensemble of 19 models, the pattern of global SST difference between large AWP years and small AWP years shown in Fig. 13b has a realistic representation of the observed AMO pattern. Compared with ERSST, 14 models—CanESM2, CSIRO Mk 3.6.0, GFDL CM3 (Fig. 13d), GFDL-ESM2G, GISS-E2H, GISS-E2R, HadGEM2-CC, INM-CM4, IPSL-CM5A-LR, IPSL-CM5A-MR, IPSL-CM5B-LR, MPI-ESM-LR, MPI-ESM-P, and NorESM1—successfully reproduce the major characteristics of the observed pattern of global SST difference between large AWP years and small AWP years. NCAR CCSM4 (Fig. 13c), GFDL-ESM2M, and MRI-CGCM3 show a global warming signature with out-of-phase cooling to the south of Greenland Island. HadCM3 and HadGEM2-ES have a significant cooling pattern in the North Pacific instead of the warming shown in most CGCMs.

d. Remote connection

Next we focus on interannual variability of the AWP induced by remote influences. AWP variability can be remotely influenced by ENSO and the NAO. Czaja et al. (2002) and Enfield et al. (2006) studied the delayed influence of ENSO and the NAO on the tropical North Atlantic region. Here we performed the same analysis as LWLE12 on the AWP region to show how this remote influence acts on the AWP in CGCMs. We regress zonally averaged observed variables including surface wind stress, net surface heat flux, and SST in the AWP region on the Niño-3 SST index (Fig. 14a1) and the negative NAO index (Fig. 14a2) from January to December. Figure 14a1

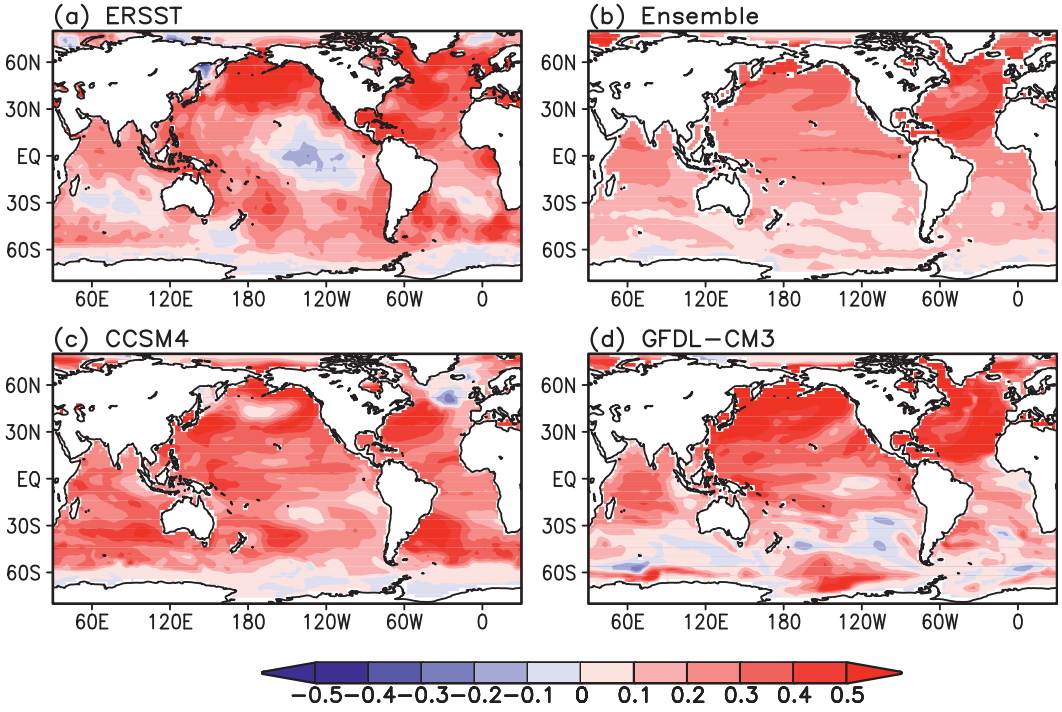

FIG. 13. Pattern of global SST difference (°C) between large AWP years and small AWP years on the decadal time scale and above. Shown are (a) ERSST, (b) ensemble of 19 models, (c) NCAR CCSM4, and (d) GFDL CM3. The threshold value of AWPTI to define large (small) AWP years is 0.1°C (−0.1°C).

shows that positive ENSO events correspond to westerly low-level wind anomalies over the AWP (shown in vectors), which are largest during January–March. This wind anomaly induces heating between 5°N and 20°N over the AWP region at a rate of 8 W m^{-2} due to a decreased latent heat loss (shown in contour) and leads to a warm SST anomaly (shown in shading) of 0.2°C during February–May (FMAM). Figure 14a2 shows a regression pattern on the negative NAO index similar to Fig. 14a1, but the magnitude of the SST warming anomaly between 5° and 20°N is about 0.2°C less than the magnitude of ENSO influence. The anomalous net heat flux also switches sign after March. The same results have been addressed in detail in LWLE12. The mechanism determining the forcing of AWP variability in spring by both ENSO and the NAO is similar to the mechanism suggested by Czaja et al. (2002) for the NTA.

Compared with the above observational analysis, the ensemble of the 19 analyzed models successfully simulates the observed remote influence pattern in the AWP region induced by both ENSO (Fig. 14b1) and the NAO (Fig. 14b2). Only four models, identified as category I, are able to successfully capture the major features for the remote influence from both ENSO and NAO influences: NCAR CCSM4 (Figs. 14c1–c2), GISS-E2H, GISS-E2R, and NorESM1-M. Four models in category II are able to capture the major character of the NAO influence: HadGEM2-CC (Fig. 14d1–d2), HadGEM2-ES, INM-CM4, and IPSL-CM5A-MR. In these models, the wind–evaporation–SST mechanism still holds valid in explaining the processes. However, the process of warming in FMAM between 5° and 20°N induced by ENSO is not captured—or captured but lasts to ASO. Category III, consisting of CanESM2, CSIRO Mk 3.6.0, GFDL CM3, GFDL-ESM2G, GFDL-ESM2M, HadCM3, IPSL-CM5A-LR, IPSL-CM5B-LR, MPI-ESM-LR, MPI-ESM-P, and MRI-CGCM3 (Fig. 14e2), is not able to successfully simulate the observed regression patterns for both ENSO and the NAO. These models either simulated a delayed warming in the ASO pattern (Fig. 14e2) or are not able to capture the warming phase between 5° and 20°N compared with observations.

In Fig. 15a, a Taylor diagram is constructed using the regression coefficients of ENSO influence shown in Fig. 14 to quantify performance of the CGCMs. The correlation between each model and observations is calculated between the regression coefficient at each grid point of model and the regression coefficient at the same grid points of observation as shown in the domain of Fig. 14a1. The standard deviation for the statistics of each model is divided by the standard deviation of observations. The reference point "A" for

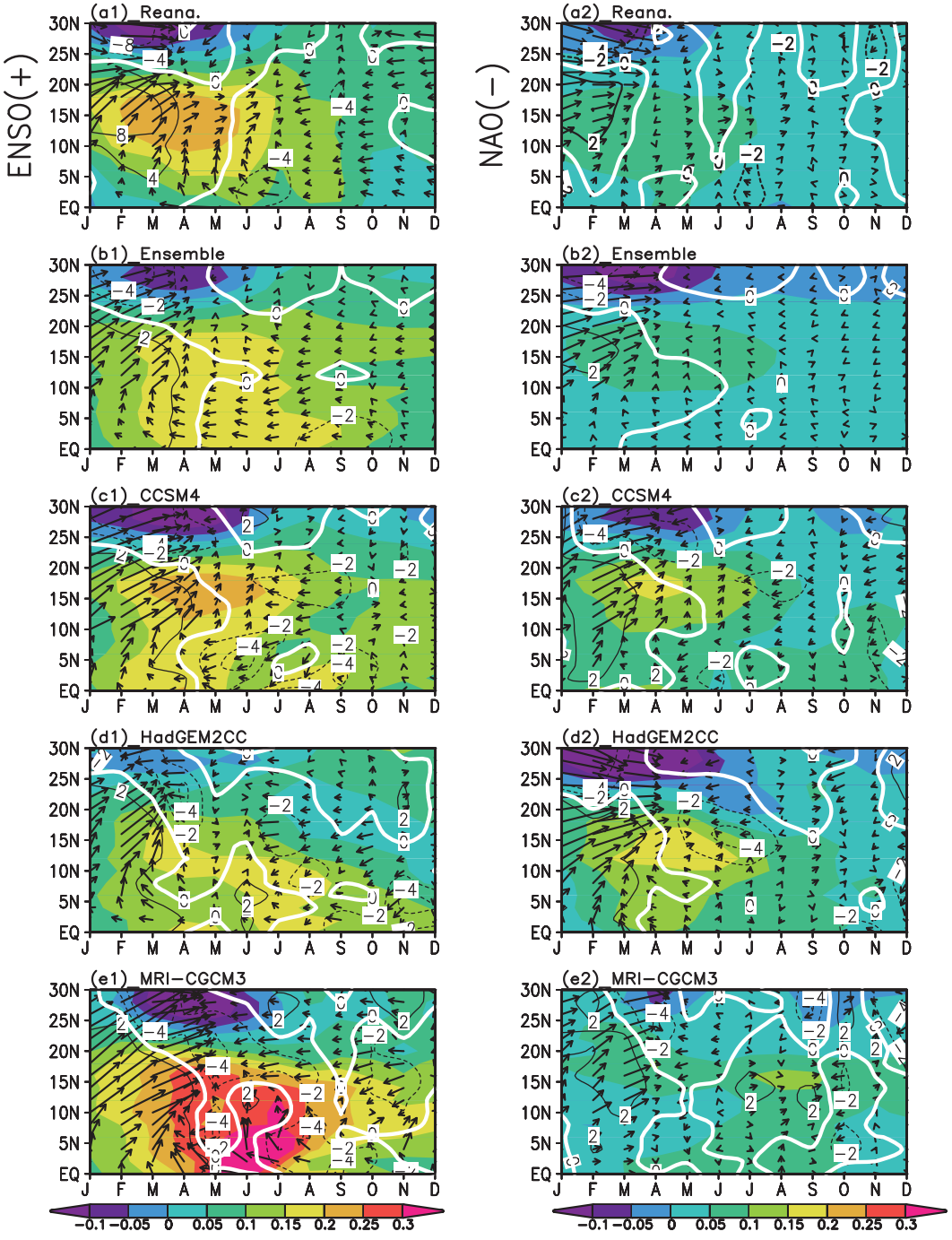

FIG. 14. Regression maps of surface wind stress (vector, N m^{-2}), net surface heat flux (positive into the ocean with solid contour line, W m^{-2}), and SST (shading contour, °C) averaged in longitude onto Niño-3 Index (DJF) and onto negative NAO index (DJFM): (a1) regression map onto Niño-3 Index for observations, (a2) regression map onto negative NAO Index for observations, (b1) regression map onto Niño-3 Index for ensemble of 19 models, and (b2) regression map onto negative NAO Index for ensemble. (c)–(e) As in (b), but for selected models.

perfect correspondence of models to observations is at the (1, 1) point of standard deviation and correlation coefficient coordinates. If the point of a model in the diagram is closer to the reference point, then the model has a better performance in representing the observed pattern.

By this metric NCAR CCSM4 (C), INM-CM4 (M), GISS-E2H (H), and NorESM1-M (T) are the models

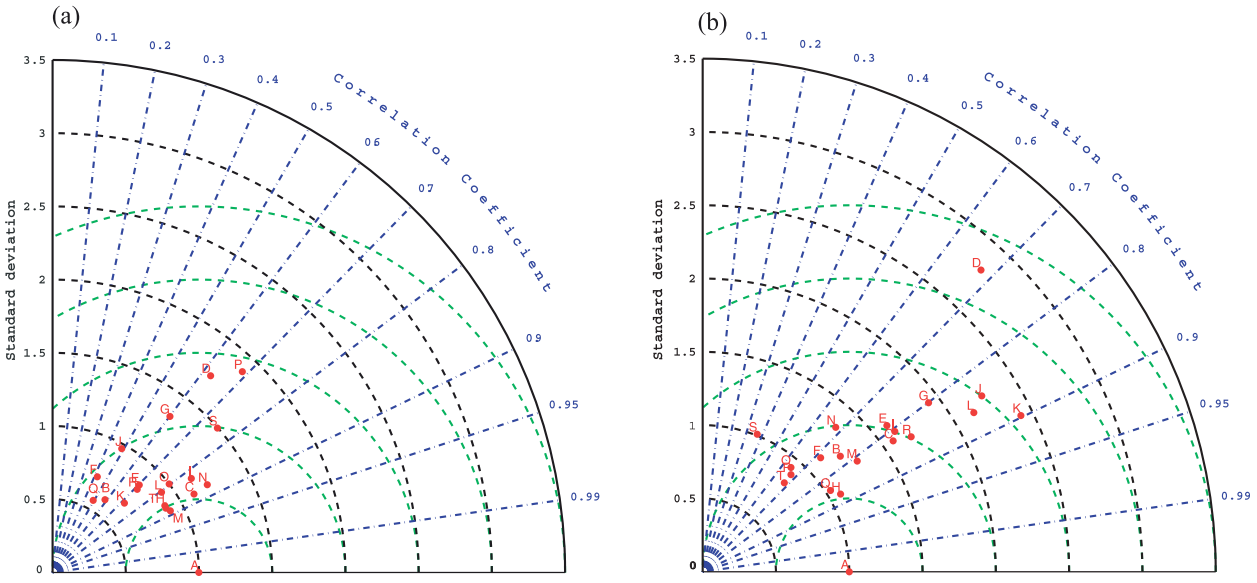

FIG. 15. (a) A Taylor diagram of statistics describing the remote influenced patterns of ENSO on AWP in CGCMs as shown in Fig. 14a1. On this diagram, the radial coordinate gives the magnitude of total standard deviation of lag regression coefficients in the domain of Fig. 14a1 for each model normalized by the standard deviation of observation, and the angular coordinate gives the correlation of the regression coefficients of each model with the regression coefficients of observation. The distance between the reference point "A" of observation and any model's point (models B–T are defined in Table 1) is proportional to the root-mean-square error shown by the green dashed lines. (b) As in (a), but the statistics of Taylor diagram describing the remote influenced patterns of NAO on AWP in CGCMs as shown in Fig. 14a2.

that best replicate the AWP connection to ENSO. Except INM-CM4, all of the other three models are categorized as the best models in earlier discussion in simulating ENSO influence on the AWP based on subjective judgment. For INM-CM4, the regression pattern of ENSO has a notable erroneous warming close to the equator, except the warming between 5° and 20°N in spring as in observations. So we regard this model as unable to simulate the ENSO influence successfully. In general, the Taylor diagram has proved to be a successful tool to quantitatively evaluate the performance of CGCMs.

Figure 15b is the same as Fig. 15a except that the statistics are defined as regression coefficients of SST onto the NAO [December–March (DJFM)] index at all grid points within the domain as shown in Fig. 14a2. GISS-E2H (H) and MPI-ESM-P (Q) are the best two models compared with the reference point for observations. MPI-ESM-P, however, has a delayed NAO influence until ASO, so it is not included as one of the best models in simulating the NAO influence in earlier discussion. Comparison between Figs. 15a and 15b indicates that the selected 19 CMIP5 CGCMs, unlike the CGCMs in CMIP3, demonstrate comparable performance in simulating the remote influence pattern in the AWP region induced by the NAO with the performance in simulating the influence induced by ENSO. This conclusion is also reflected in the regression patterns of the model ensemble mean in Fig. 14b1 and 14b2.

5. Summary and discussion

In this paper we explore AWP variability in 19 CGCMs from the CMIP5 database and validate them against observations over the twentieth century at the seasonal, interannual, and multidecadal time scales, as well as for the remote connections with ENSO and the NAO. Both the AWPAI and AWPTI are defined to study the seasonal cycle. Seven models—NCAR CCSM4, CSIRO Mk 3.6.0, GISS-E2H, GISS-E2R, HadCM3, MPI-ESM-LR, and MPI-ESM-P—have the best performance in simulating the AWP seasonal cycle based on both indexes. The AWPAI is almost zero for some models in most years due to cold SST bias found in the northern tropics for most models. Thus, we have chosen an SST index as a more effective but equivalent proxy for AWP variability. Only NCAR CCSM4 and GISS-E2H are able to capture all the first four modes of ERSST rEOF. Analysis of the AWP remote connection with ENSO and the NAO shows that NCAR CCSM4, GISS-E2H, GISS-E2R, and NorESM1-M are the best group of models in simulating the processes by which ENSO and NAO influence the AWP region through wind–evaporation–SST interactions. Fourteen models listed in Table 3 successfully capture the spatial characters of global SST between large AWP years and small AWP years. All the best models in each evaluation aspect are summarized in Table 3. NCAR CCSM4, GISS-E2H, and GISS-E2R are

TABLE 3. Summary of best performance models in each aspect of variability evaluation.

Criterion	Best performance models
Seasonal cycle	NCAR CCSM4, CSIRO Mk 3.6.0, GISS-E2H, GISS-E2R, HadCM3, MPI-ESM-LR, MPI-ESM-P
rEOF analysis	NCAR CCSM4, GISS-E2H
Multidecadal variability (roughly estimated)	CanESM2, CSIRO Mk 3.6.0, GFDL CM3, GFDL-ESM2G, GISS-E2H, GISS-E2R, HadGEM2-CC, INM-CM4, IPSL-CM5A-LR, IPSL-CM5A-MR, IPSL-CM5B-LR, MPI-ESM-LR, MPI-ESM-P, NorESM1-M
Remote connection with ENSO and NAO	NCAR CCSM4, GISS-E2H, GISS-E2R, NorESM1-M

the best models in simulating the AWP variability based on this study. The previous generation of models developed at NCAR and GISS (CCSM3, GISS-ER, and GISS-AOM) are quite limited in AWP simulation (LWLE12) and hence are much improved in their CMIP5 reincarnation. As the physics and configuration for every CGCM are improved and more complex compared with CMIP3 CGCMs, the results presented in this study provide a useful reference in continuing to improve CGCM simulations of the AWP.

As discussed with respect to the AWP seasonal cycle, the cold SST bias in the AWP region still exists in most CMIP5 CGCMs. The pattern of the warm SST bias in the cold tongue and Angola–Namibia region and cold bias in the NTA is a ubiquitous feature of most CGCMs from both CMIP3 and CMIP5. The analysis of NTA SST bias in the study of Grodsky et al. (2012) showed that the atmospheric components of CCSM3 and CCSM4 have abnormally intense subtropical high pressure systems and abnormally weak subpolar low pressure systems, and these SLP biases cause excessively strong surface winds and result in too large latent heat loss and cold SST bias throughout the NTA basin. We examine this process among 19 CGCMs of CMIP5 and we find that excessively strong subtropical highs are able to explain the cold SST bias in the NTA region for most CGCMs. However, a positive bias in the North Atlantic subtropical high (NASH) is unable to explain the cold SST bias in the AWP region because the excess latent heat loss is much smaller compared with observations possibly due to weaker sea surface specific humidity gradient. We adopt the same latent heat flux dataset (IFREMER) used in Grodsky et al. (2012) as an observation reference instead of the latent heat flux data from 20CR for consistency. However, if we use the latent heat flux data of 20CR and NCEP reanalysis datasets as reference, the excess latent heat loss is also much smaller in the AWP region (not shown) and our conclusion is consistency among these different datasets.

We find that among the CGCMs of CMIP5, SST is positively correlated with high-level cloud fraction and downward longwave radiation in the AWP region. It indicates that lower (higher) AWP SST contributes to less (more) high-level cloud fraction and thus leads to less (more) reflected downward longwave radiation. The decreased (increased) longwave radiation can further decrease (warm) the AWP SST. This positive feedback may erroneously alleviate the AWP SST cold bias when excessively high-level clouds are simulated. The origin of the cold bias in the AWP is still uncertain. A recently published paper of Fasullo and Trenberth (2012) suggests that the present models with low climate sensitivity perform more inadequately in replicating climate teleconnections between the tropics and subtropics, and are identifiably biased. They pointed out that the relative contributions of various cloud types to the overall cloud feedback and the sources of biases in the vertical relative humidity and cloud distributions in models are two of major questions to be solved for correctly simulating climate sensitivity. These two questions may also be of fundamental importance to trace the origin of the topical SST bias in models.

Acknowledgments. We acknowledge the World Climate Research Programme's Working Group on Coupled Modelling, which is responsible for CMIP, and we thank the climate modeling groups (listed in Table 1 of this paper) for producing and making available their model output. For CMIP the U.S. Department of Energy's Program for Climate Model Diagnosis and Intercomparison provides coordinating support and led development of software infrastructure in partnership with the Global Organization for Earth System Science Portals. We thank Gregory Foltz, Marlos Goes, Lei Zhou, and three anonymous reviewers for their thoughtful comments and suggestions. This work was supported by grants from the National Oceanic and Atmospheric Administration's Climate Program Office and by grants from the National Science Foundation.

APPENDIX

List of Institutional Model Acronyms and Names

CanESM2	Canadian Earth System Model, version 2
CCSM3	NCAR Community Climate System Model version 3

CCSM4	NCAR Community Climate System Model version 4
CSIRO Mk3.6	Commonwealth Scientific and Industrial Research Organisation Mark version 3.6
GFDL CM2	Geophysical Fluid Dynamics Laboratory (GFDL) Climate Model version 2.0
GFDL CM3	GFDL Climate Model version 3.0
GFDL-ESM2G	GFDL Earth Science Model 2G
GFDL-ESM2M	GFDL Earth Science Model 2M
GISS-AOM	Goddard Institute for Space Studies (GISS) Atmosphere–Ocean Model
GISS-E2H	GISS Model E, version 2, coupled with the Hybrid Coordinate Ocean Model (HYCOM) ocean model
GISS-E2R	GISS model E, version 2, coupled with the Russell ocean model
HadCM3	Third climate configuration of the Met Office Unified Model
HadGEM2-CC	Hadley Centre Global Environmental Model 2, Carbon Cycle
HadGEM2-ES	Hadley Centre Global Environmental Model 2, Earth System
INM-CM4	Institute of Numerical Mathematics Coupled Model, version 4.0
IPSL CM4	L'Institut Pierre-Simon Laplace (IPSL) Coupled Model, version 4
IPSL-CM5A-LR	IPSL Coupled Model, version 5, coupled with NEMO, low-resolution
IPSL-CM5A-MR	IPSL Coupled Model, version 5, coupled with NEMO, medium-resolution
IPSL-CM5B-LR	IPSL Coupled Model, version 5
MPI-ESM-LR	Max Planck Institute (MPI) Earth System Model, low resolution
MPI-ESM-P	MPI Earth System Model
MRI-CGCM3	Meteorological Research Institute Coupled General Circulation Model, version 3
NorESM1-M	Norwegian Earth System Model, intermediate resolution

REFERENCES

Bates, S. C., 2008: Coupled ocean–atmosphere interaction and variability in the tropical Atlantic Ocean with and without an annual cycle. *J. Climate,* **21,** 5501–5523.

Bell, G. D., and M. Chelliah, 2006: Leading tropical modes associated with interannual and multidecadal fluctuations in North Atlantic hurricane activity. *J. Climate,* **19,** 590–612.

Bentamy, A., L. H Ayina, W. Drennan, K. Katsaros, A. M. Mestas-Nunez, and R. T. Pinker, 2008: 15 years of ocean surface momentum and heat fluxes from remotely sensed observations. *FLUX NEWS,* No. 5, WCRP Working Group on Surface Fluxes, 14–16. [Available online at sail.msk.ru/newsletter/fluxnews_5_final.pdf.]

Carton, J. A., and B. H. Huang, 1994: Warm events in the tropical Atlantic. *J. Phys. Oceanogr.,* **24,** 888–903.

Chang, C.-Y., J. A. Carton, S. A. Grodsky, and S. Nigam, 2007: Seasonal climate of the tropical Atlantic sector in the NCAR Community Climate System Model 3: Error structure and probable causes of errors. *J. Climate,* **20,** 1053–1070.

——, S. Nigam, and J. A. Carton, 2008: Origin of the spring-time westerly bias in equatorial Atlantic surface winds in the Community Atmosphere Model version 3 (CAM3) simulation. *J. Climate,* **21,** 4766–4778.

Chang, P., L. Ji, and H. Li, 1997: A decadal climate variation in the tropical Atlantic Ocean from thermodynamic air–sea interactions. *Nature,* **385,** 516–518.

Compo, G. P., and Coauthors, 2011: The Twentieth Century Reanalysis Project. *Quart. J. Roy. Meteor. Soc.,* **137,** 1–28, doi:10.1002/qj.776.

Czaja, A., and J. Marshall, 2001: Observations of atmosphere–ocean coupling in the North Atlantic. *Quart. J. Roy. Meteor. Soc.,* **127,** 1893–1916.

——, P. van der Vaart, and J. Marshall, 2002: A diagnostic study of the role of remote forcing in tropical Atlantic variability. *J. Climate,* **15,** 3280–3290.

Delworth, T. L., and M. E. Mann, 2000: Observed and simulated multidecadal variability in the Northern Hemisphere. *Climate Dyn.,* **16,** 661–676.

de Szoeke, S. P., and S.-P. Xie, 2008: The tropical eastern Pacific seasonal cycle: Assessment of errors and mechanisms in IPCC AR4 coupled ocean–atmosphere general circulation models. *J. Climate,* **21,** 2573–2590.

Doi, T., T. Tozuka, and T. Yamagata, 2010: The Atlantic meridional mode and its coupled variability with the Guinea Dome. *J. Climate,* **23,** 455–475.

Donner, L. J., and Coauthors, 2011: The dynamical core, physical parameterizations, and basic simulation characteristics of the atmospheric component AM3 of the GFDL global coupled model CM3. *J. Climate,* **24,** 3484–3519.

Enfield, D. B., and S.-K. Lee, 2005: The heat balance of the Western Hemisphere warm pool. *J. Climate,* **18,** 2662–2681.

——, and L. Cid-Serrano, 2010: Secular and multidecadal warmings in the North Atlantic and their relationships with major hurricane activity. *Int. J. Climatol.,* **30,** 174–184, doi:10.1002/joc.1881.

——, A. M. Mestas-Nuñez, D. A. Mayer, and L. Cid-Serrano, 1999: How ubiquitous is the dipole relationship in tropical Atlantic sea surface temperatures? *J. Geophys. Res.,* **104** (C4), 7841–7848, doi:10.1029/1998JC900109.

——, ——, and P. J. Trimble, 2001: The Atlantic multidecadal oscillation and its relation to rainfall and river flows in the continental U.S. *Geophys. Res. Lett.,* **28,** 2077–2080.

——, S.-K. Lee, and C. Wang, 2006: How are large Western Hemisphere warm pools formed? *Prog. Oceanogr.,* **70,** 346–365.

Fasullo, T. T., and K. E. Trenberth, 2012: A less cloudy future: The role of subtropical subsidence in climate sensitivity. *Science,* **338,** 792–794.

Goldenberg, S. B., C. W. Landsea, A. M. Mesta-Nunez, and W. M. Gray, 2001: The recent increase in Atlantic hurricane activity: Causes and implications. *Science,* **293,** 474–479.

Grodsky, S. A., J. A. Carton, S. Nigam, and Y. M. Okumura, 2012: Tropical Atlantic biases in CCSM4. *J. Climate,* **25,** 3684–3701.

Hu, Z.-Z., B. Huang, and K. Pegion, 2008: Leading patterns of the tropical Atlantic variability in a coupled general circulation model. *Climate Dyn.,* **30,** 703–726.

Huang, B., and J. Shukla, 2005: Ocean–atmosphere interactions in the tropical and subtropical Atlantic Ocean. *J. Climate,* **18,** 1652–1672.

——, P. S. Schopf, and J. Shukla, 2004: Intrinsic ocean–atmosphere variability of the tropical Atlantic Ocean. *J. Climate,* **17,** 2058–2077.

Hurrell, J. W., 1995: Decadal trends in the North Atlantic Oscillation: Regional temperatures and precipitation. *Science,* **269,** 676–679.

Jiang, J. H., and Coauthors, 2012: Evaluation of cloud and water vapor simulations in CMIP5 climate models using NASA ''A-Train'' satellite observations. *J. Geophys. Res.,* **117,** D14105, doi:10.1029/2011JD017237.

Joseph, R., and S. Nigam, 2006: ENSO evolution and teleconnections in IPCC's twentieth-century climate simulations: Realistic representation? *J. Climate,* **19,** 4360–4377.

Large, W. G., G. Danabasoglu, 2006: Attribution and impacts of upper-ocean biases in CCSM3. *J. Climate,* **19,** 2325–2346.

Latif, M., and A. Grötzner, 2000: The equatorial Atlantic oscillation and its response to ENSO. *Climate Dyn.,* **16,** 213–218.

Lee, S.-K., D. B. Enfield, and C. Wang, 2007: What drives the seasonal onset and decay of the Western Hemisphere warm pool? *J. Climate,* **20,** 2133–2146.

Li, G., and S.-P. Xie, 2012: Origins of tropical-wide SST biases in CMIP multi-model ensembles. *Geophys. Res. Lett.,* **39,** L22703, doi:10.1029/2012GL053777.

Liu, H., C. Wang, S. Lee, and D. Enfield, 2012: Atlantic warm-pool variability in the IPCC AR4 CGCM simulations. *J. Climate,* **25,** 5612–5628.

Meehl, G. A., C. Covey, K. E. Taylor, T. Delworth, R. J. Stouffer, M. Latif, B. McAvaney, and J. F. B. Mitchell, 2007: The WCRP CMIP3 multimodel dataset: A new era in climate change research. *Bull. Amer. Meteor. Soc.,* **88,** 1383–1394.

Misra, V., S. Chan, R. Wu, and E. Chassignet, 2009: Air–sea interaction over the Atlantic warm pool in the NCEP CFS. *Geophys. Res. Lett.,* **36,** L15702, doi:10.1029/2009GL038737.

Muñoz, E., W. Weijer, S. A. Grodsky, S. C. Bates, and I. Wainer, 2012: Mean and variability of the tropical Atlantic Ocean in the CCSM4. *J. Climate,* **25,** 4860–4882.

Okumura, Y., and S.-P. Xie, 2006: Some overlooked features of tropical Atlantic climate leading to a new Niño-like phenomenon. *J. Climate,* **19,** 5859–5874.

Philander, S. G. H., 1986: Predictability of El Niño. *Nature,* **321,** 810–811.

Richter, I., and S.-P. Xie, 2008: On the origin of equatorial Atlantic biases in coupled general circulation models. *Climate Dyn.,* **31,** 587–598.

——, ——, A. T. Wittenberg, and Y. Masumoto, 2012: Tropical Atlantic biases and their relation to surface wind stress and terrestrial precipitation. *Climate Dyn.,* **38,** 985–1001, doi:10.1007/s00382-011-1038-9.

Saji, N. H., S.-P. Xie, and T. Yamagata, 2006: Tropical Indian Ocean variability in the IPCC 20th-century climate simulations. *J. Climate,* **19,** 4397–4417.

Servain, J., 1991: Simple climatic indices for the tropical Atlantic Ocean and some applications. *J. Geophys. Res.,* **96** (C8), 15 137–15 146.

Smith, T. M., R. W. Reynolds, T. C. Peterson, and J. Lawrimore, 2008: Improvements to NOAA's historical merged land–ocean surface temperature analysis (1880–2006). *J. Climate,* **21,** 2283–2296.

Su, H., and Coauthors, 2008: Variations of tropical upper tropospheric clouds with sea surface temperature and implications for radiative effects. *J. Geophys. Res.,* **113,** D10211, doi:10.1029/2007JD009624.

Taylor, K. E., 2001: Summarizing multiple aspects of model performance in a single diagram. *J. Geophys. Res.,* **106** (D7), 7183–7192, doi:10.1029/2000JD900719.

Torrence, C., and G. P. Compo, 1998: A practical guide to wavelet analysis. *Bull. Amer. Meteor. Soc.,* **79,** 61–78.

Tozuka, T., T. Doi, T. Miyasaka, N. Keenlyside, and T. Yamagata, 2011: Key factors in simulating the equatorial Atlantic zonal sea surface temperature gradient in a coupled general circulation model. *J. Geophys. Res.,* **116,** C06010, doi:10.1029/2010JC006717.

Wang, C., and D. B. Enfield, 2001: The tropical Western Hemisphere warm pool. *Geophys. Res. Lett.,* **28,** 1635–1638.

——, and ——, 2003: A further study of the tropical Western Hemisphere warm pool. *J. Climate,* **16,** 1476–1493.

——, ——, S.-K. Lee, and C. W. Landsea, 2006: Influences of the Atlantic warm pool on Western Hemisphere summer rainfall and Atlantic hurricanes. *J. Climate,* **19,** 3011–3028.

——, S.-K. Lee, and D. B. Enfield, 2008a: Atlantic warm pool acting as a link between Atlantic multidecadal oscillation and Atlantic tropical cyclone activity. *Geochem. Geophys. Geosyst.,* **9,** Q05V03, doi:10.1029/2007GC001809.

——, ——, and ——, 2008b: Climate response to anomalously large and small Atlantic warm pools during the summer. *J. Climate,* **21,** 2437–2450.

——, H. Liu, S.-K. Lee, and R. Atlas, 2011: Impact of the Atlantic warm pool on United States landfalling hurricanes. *Geophys. Res. Lett.,* **38,** L19702, doi:10.1029/2011GL049265.

Wang, X., D. Wang, and W. Zhou, 2009: Decadal variability of twentieth century El Niño and La Niña occurrence from observations and IPCC AR4 coupled models. *Geophys. Res. Lett.,* **36,** L11701, doi:10.1029/2009GL037929.

Wu, R., B. P. Kirtman, and K. Pegion, 2006: Local air–sea relationship in observations and model simulations. *J. Climate,* **19,** 4914–4932.

Xie, S.-P., and J. A. Carton, 2004: Tropical Atlantic variability: Patterns, mechanisms, and impacts. *Earth's Climate: The Ocean–Atmosphere Interaction, Geophys. Monogr.,* Vol. 147, Amer. Geophys. Union, 121–142.

——, Y. Tanimoto, H. Noguchi, and T. Matsuno, 1999: How and why climate variability differs between the tropical Atlantic and Pacific. *Geophys. Res. Lett.,* **26,** 1609–1612, doi:10.1029/1999GL900308.

Zebiak, S. E., 1993: Air–sea interaction in the equatorial Atlantic region. *J. Climate,* **6,** 1567–1586.